Applied Geochemistry 135 (2021) 105114

Contents lists available at ScienceDirect

Applied Geochemistry

journal homepage: www.elsevier.com/locate/apgeochem

Synergetic Tl and As retention in secondary minerals: An example of extreme arsenic and thallium pollution

Tamara Đorđević [a,*], Petr Drahota [b], Uwe Kolitsch [c,a], Juraj Majzlan [d], Magdaléna Peřestá [b], Stefan Kiefer [d], Michael Stöger-Pollach [e], Nathalie Tepe [f], Thilo Hofmann [f], Tomáš Mikuš [g], Goran Tasev [h], Todor Serafimovski [h], Ivan Boev [h], Blažo Boev [h]

[a] Institut für Mineralogie und Kristallographie, Universität Wien, Althanstr. 14, A-1090 Wien, Austria
[b] Institute of Geochemistry, Mineralogy and Mineral Resources, Faculty of Science, Charles University, Albertov 6, 128 43 Prague 2, Czech Republic
[c] Mineralogisch-Petrographische Abteilung, Naturhistorisches Museum, Burgring 7, A-1010 Wien, Austria
[d] Institute of Geosciences, Department of Mineralogy, Friedrich-Schiller-Universität, Carl-Zeiss-Promenade 10, 07745 Jena, Germany
[e] University Service Centre for TEM, Technische Universität Wien, Wiedner Hauptstr. 8-10, A-1040 Wien, Austria
[f] Environmental Geosciences, Centre for Microbiology and Environmental Systems Science, University of Vienna, Althanstr. 14, A-1090 Wien, Austria
[g] Earth Science Institute, Slovak Academy of Sciences, Geological Division, Ďumbierska 1, 974 01 Banská Bystrica, Slovakia
[h] Faculty of Natural Sciences, University "Goce Delčev"-Štip, Goce Delčev 89, 2000 Štip, Macedonia

ARTICLE INFO

Editorial handling by Prof. M. Kersten

Keywords:
Thallium arsenates
Thallium sulfates
Speciation
Structural incorporation
Soil pollution

ABSTRACT

Secondary minerals could be effective scavengers of toxic arsenic (As) and thallium (Tl). In environments polluted by mining, these elements are abundant both in acid rock/mine drainage scenarios, as well as in carbonate-buffered environments. In this study we have investigated the behavior of As and Tl during weathering in mine waste dumps and an associated technosol sample from the Crven Dol locality (Allchar Tl–As–Sb–Au deposit, North Macedonia) contaminated with up to 142 g kg^{-1} of As and 18 g kg^{-1} of Tl, making it an As- and Tl-extreme environment. We identified As and Tl reservoirs and discuss their difference from those observed in other naturally As- and Tl-rich environments. The pore waters show high concentrations of As (up to 196 mg L^{-1}) and Tl (up to 660 μg L^{-1}). Mild extractions mobilized up to 46% of the total Tl and 11% of the total As, indicating that a large amount of these toxic elements is weakly bound and can be easily mobilized into the environment. Apart from the recognition of Tl storage in several secondary phases (mainly as Tl(I) in members of the pharmacosiderite and jarosite groups, as well as Mn oxides, but also as very minor Tl(III) in other secondary phases), this study also provides the first evidence of Tl uptake by previously unknown thallium arsenate phases (with Tl: As ratios ~ 2 and 4), detected in carbonate-buffered (near-neutral pH) As- and Tl-rich technosols and waste dumps. These results indicate the need for further studies on Tl speciation in extremely As- and Tl-rich environments.

1. Introduction

Both historical and modern metal mining areas and accompanying waste material related to the extraction and processing of ore very often contain considerable amounts of heavy metals and metalloids. These sites represent one of the most important latent hazards for water, soils, biodiversity, and the food chain. They are due to continuous metal release from mechanically unstable, chemically labile, and non-remediated mine tailings and from abandoned former mine sites where waste materials are subjected to atmospheric conditions, runoffs (underground or meteoric waters), or biotic effects (organisms living on the site or nearby) (Hudson-Edwards, 2016). Some of these elements, such as arsenic (As) and thallium (Tl) may often occur together and may mobilize and disperse extensively into surrounding areas. Their environmental behavior is controlled by several factors, such as mineralogy of the primary ores and country rocks, weathering conditions, transformations to secondary minerals, and changeability in hydrogeology. High concentrations of As and Tl can be naturally attenuated by a series of pH-buffering, precipitation, and sorption reactions, particularly significant when fresh secondary solid phases are formed (Carbone et al., 2013).

* Corresponding author.
E-mail address: tamara.djordjevic@univie.ac.at (T. Đorđević).

https://doi.org/10.1016/j.apgeochem.2021.105114
Received 16 July 2021; Received in revised form 15 October 2021; Accepted 16 October 2021
Available online 21 October 2021

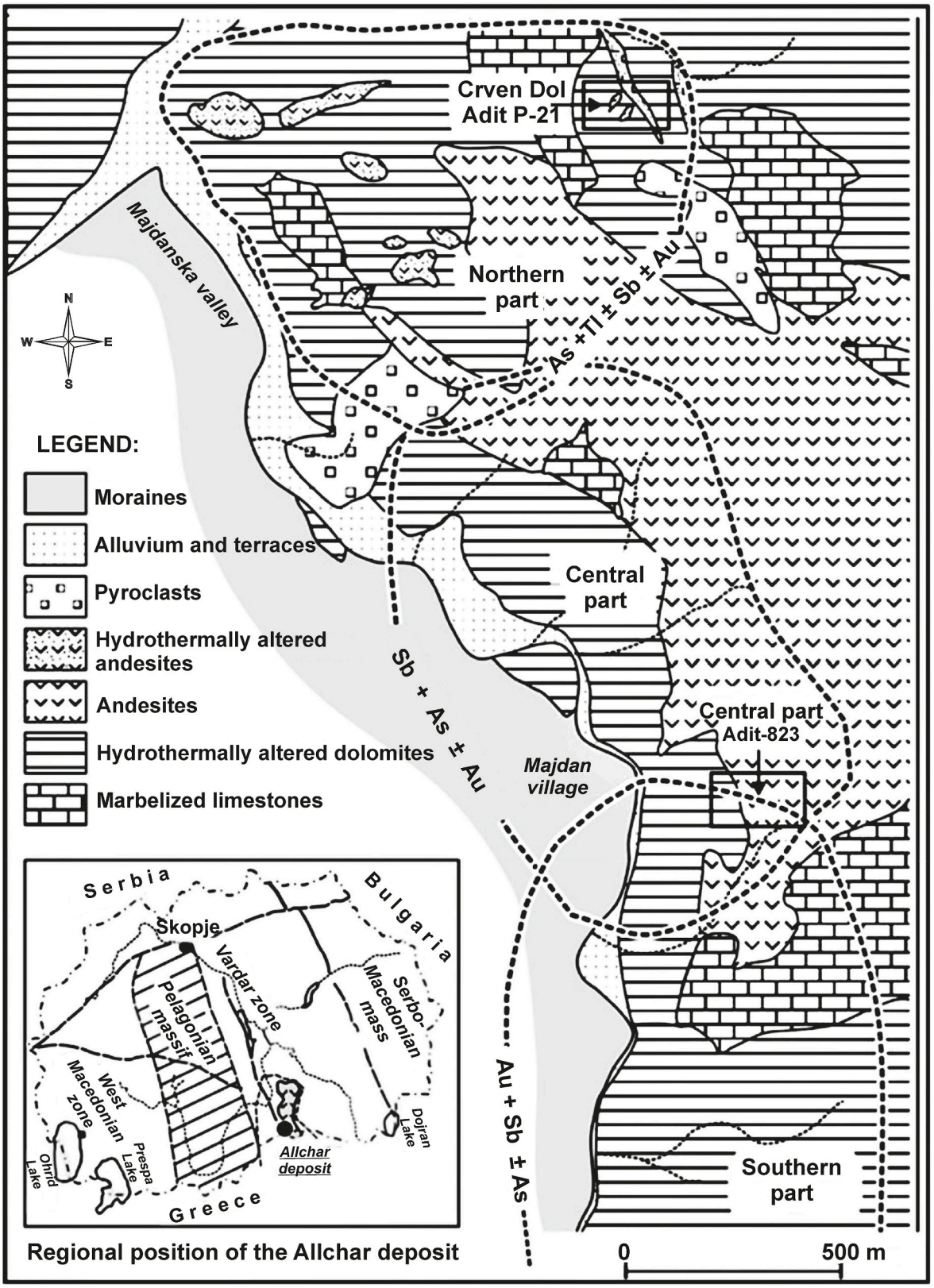

Fig. 1. Geological map of the Allchar Tl–Sb–Au deposit, North Macedonia.

A large number of secondary arsenic minerals have been found in highly contaminated soils, stream sediments, former industrial sites, and mine tailings (Craw and Bowell, 2014 and references therein). On the contrary, the behavior of thallium during weathering processes in mining-affected environments is poorly studied. There, it is often dispersed as a trace element in primary sulfides (marcasite, pyrite, galena, sphalerite, stibnite, realgar) and sulfosalts (geocronite, boulangerite, jordanite), but it can also be a major and essential element in

some rare primary thallium sulfosalts (*i.e.*, lorándite, bernardite, pierrotite, and others). In the weathering zones and affected soils, thallium is bound by secondary minerals such as avicennite (Tl_2O_3), jarosite-group minerals (Balić-Žunić et al., 1994; Hermann et al., 2018; Aguilar-Carrillo et al., 2020), members of the pharmacosiderite group (Balić-Žunić et al., 1993), clay minerals (Martin et al., 2018; Wick et al., 2018), as well as iron and manganese oxyhydroxides (Gołębiowska et al., 2016; Voegelin et al., 2015; Wick et al., 2019; Aguilar-Carrillo et al., 2018, 2020; López-Arce et al., 2019).

There are only few larger Tl accumulations in the world (always accompanied by As mineralization) that could potentially serve as sources of this rare and toxic metal. The most important ones comprise the famous Xiangquan and Lanmuchang deposits in China (Liu et al. 2019, 2020; Lee et al., 2019; Lin et al., 2020), several Carlin-type gold deposits in Nevada, USA, the famous Lengenbach deposit in Switzerland (Hofmann and Knill, 1996; Raber and Roth, 2018), the Jas Roux occurrence in the French Alps (Johan und Manntiene, 2000), and the Allchar (Carlin-type Tl–As–Sb–Au) deposit in North Macedonia (Janković, 1993; Rieck, 1993; Percival and Radtke, 1994; Strmić Palinkaš et al., 2018).

Besides its unique mineral composition and high thallium grades of the ore, the Allchar deposit probably reflects one of the highest documented Tl-concentration in technosols worldwide, with up to 20 000 mg/kg (median 660 mg/kg) (Bačeva et al., 2014a), which by far exceeds the typical Tl content in soil of <1 mg/kg (Karbowska, 2016). The highest Tl contents have been measured in the soils at the Crven Dol locality in the northern, Tl- and As-rich part of the Allchar deposit. To our best knowledge, no studies dealing with the health effects of As and Tl in the Allchar area exist. However, there are studies on the influence of the extreme metalloid and heavy metal concentrations on the local biota, such as mosses (Bačeva et al., 2013), endemic plant species (Bačeva et al., 2014b; Bačeva Andonovska et al., 2018), as well as algae and bacteria (Bermanec et al., 2018, 2021).

In this work, we studied the speciation of As and Tl in mine dumps and their cover soils (technosols) from the Crven Dol locality, Allchar deposit, North Macedonia. We focus on the composition and structure of secondary As- and Tl-bearing minerals using a broad range of mineralogical techniques (X-ray diffraction, scanning electron microscopy, electron microprobe analysis, Raman spectroscopy, transmission electron microscopy). These secondary phases were further interpreted in terms of their role as potential hosts for As and Tl in mine wastes and contaminated soils at similar sites worldwide. Finally, we combined the results from mineralogical studies, chemical extractions, and measurements of pore waters in order to model the evolution of the pore waters and assess the potential of these sites to contaminate the local environments.

2. Materials and methods

2.1. Site description

The abandoned Allchar mine is located near the hamlet of Majdan at the north-western margins of the Kožuf Mountains, 110 km SE from Skopje, North Macedonia (Fig. 1). Considering its mineral composition, the Allchar Tl–As–Sb–Au deposit is one of the highly unique ore deposits in the world. It contains exceptionally high thallium grades in comparison to worldwide accumulations of this metal. Besides economically significant Sb (stibnite) and As (realgar) concentrations, the Allchar deposit is the first Carlin-type gold deposit found in the Balkan Peninsula during the mid 1980s (Percival and Radtke, 1994; Volkov et al., 2006; Boev et al., 2012; Strmić Palinkaš et al., 2018).

The deposit was a source of As (since the 15th century) and subsequently also Sb, with a few breaks (between 1881 and 1973). In the late 1980s, special interest for thallium as a possible solar neutrino detector gave a new impulse for systematic investigations of the thallium mineralization in the northern part of the Allchar deposit, at the Crven Dol ore body (Amthauer et al., 2012; Pavićević et al., 2010 and references therein).

During the period between 1986 and 1989, gold mineralization at Allchar was systematically explored. The results of the studies showed that the geological, geochemical, mineralogical, and hydrothermal alteration features are strikingly similar to those which characterize Carlin-type mineralization of the western United States (Percival and Radtke, 1994; Strmić Palinkaš et al., 2018). Unlike the Carlin-type gold deposits in the western USA, the Allchar mineralization is hosted not only by sediments, but also by volcanics.

The mineralization of Allchar is closely related to a Pliocene volcanic complex (altered latite, dacite, and andesite) and the host rocks are dominated by Triassic carbonates (dolomite and marble) overlain by a Tertiary volcano-sedimentary sequence of tuffs and dolomites (Fig. 1). Silicification and argillitization are the most predominant alteration processes, and quartz is very abundant in hydrothermally altered volcanoclastic rocks (Janković, 1993; Percival and Radtke 1994; Pavićević et al., 2006).

The major metals and metalloids of the Allchar deposit are Fe, As, Sb, and Tl, which are accompanied by minor Au, Hg and Ba, and traces of Pb, Zn, and Cu. Enrichment of Tl in the Allchar deposit is closely associated with increased concentrations of As, Sb, and Hg. The main minerals of the deposit are pyrite, marcasite, stibnite, realgar, and orpiment, all hosted by a gangue of either dolomite or fine-grained quartz. The main primary Tl mineral is lorándite, $TlAsS_2$, but 14 other primary Tl ore minerals have been described. The Allchar area is enriched in toxic elements (As, Tl) both due to geogenic processes and a history of more than 600 years of mining.

The Allchar orebodies are composed of primary and secondary minerals, but the mineralogical composition, especially the pronounced secondary phase assemblages (Rieck, 1993), is far from being fully investigated.

Mineralization at Allchar occurs within three, not sharply defined zones (Janković and Jelenković, 1994): (i) the southern, high-temperature zone, with the dominance of Au mineralization accompanied by variable amounts of As and Sb; (ii) the central zone dominated by Sb and Au, and accompanied by As, Tl, minor Ba, Hg, and traces of Pb, and (iii) the northern zone, with a prevalence of As–Tl mineralization accompanied by minor Sb, locally with traces of Hg and Au. The Crven Dol locality belongs to the northern zone of the Allchar deposit and comprises several entrances to the underground mine (adits). Most of them collapsed and only the adit 21 is currently partly accessible and is surrounded by various waste dumps and weathered outcrops.

2.2. Sample collection and sample properties

All samples were collected at four waste dumps with associated soil outcrops. These four locations are within 150 m of each other (average GPS coordinates: N 41°09′33.80″; E 21°57′06.20″). First, using a shovel and a spade, we dug out excavation pits and/or semi-profiles at the four locations (Fig. 2b–e). Two semi-profiles (samples CD-1 and CD-2) were dug out through the yellowish grey, porous, and fine-grained mine-dump material (near to the entrance to the adit 21) (Fig. 2b and c). The third sample was collected at a realgar-rich and lorándite-bearing, strongly weathered and compacted waste dump (sample CD-3; Fig. 2d), which was overgrown by a thin layer of mosses. This waste dump is located approximately 50 m downhill from the entrance to the adit 21 and forms the southern part of the bank of a streamlet that drains the mentioned mine dump further up; this streamlet was mostly dry during the sampling period. The fourth sample (CD-4) was taken from an excavation hole dug out in the soil (technosol) in the streamlet bed, 30 m further downhill from the third site, where the run-off waters extensively gather in the streamlet, and flow further in the direction of the Majdanska river, along the eastern bank of which further collapsed adits and dumps are located (sample CD-4; Fig. 2e). These sediments are

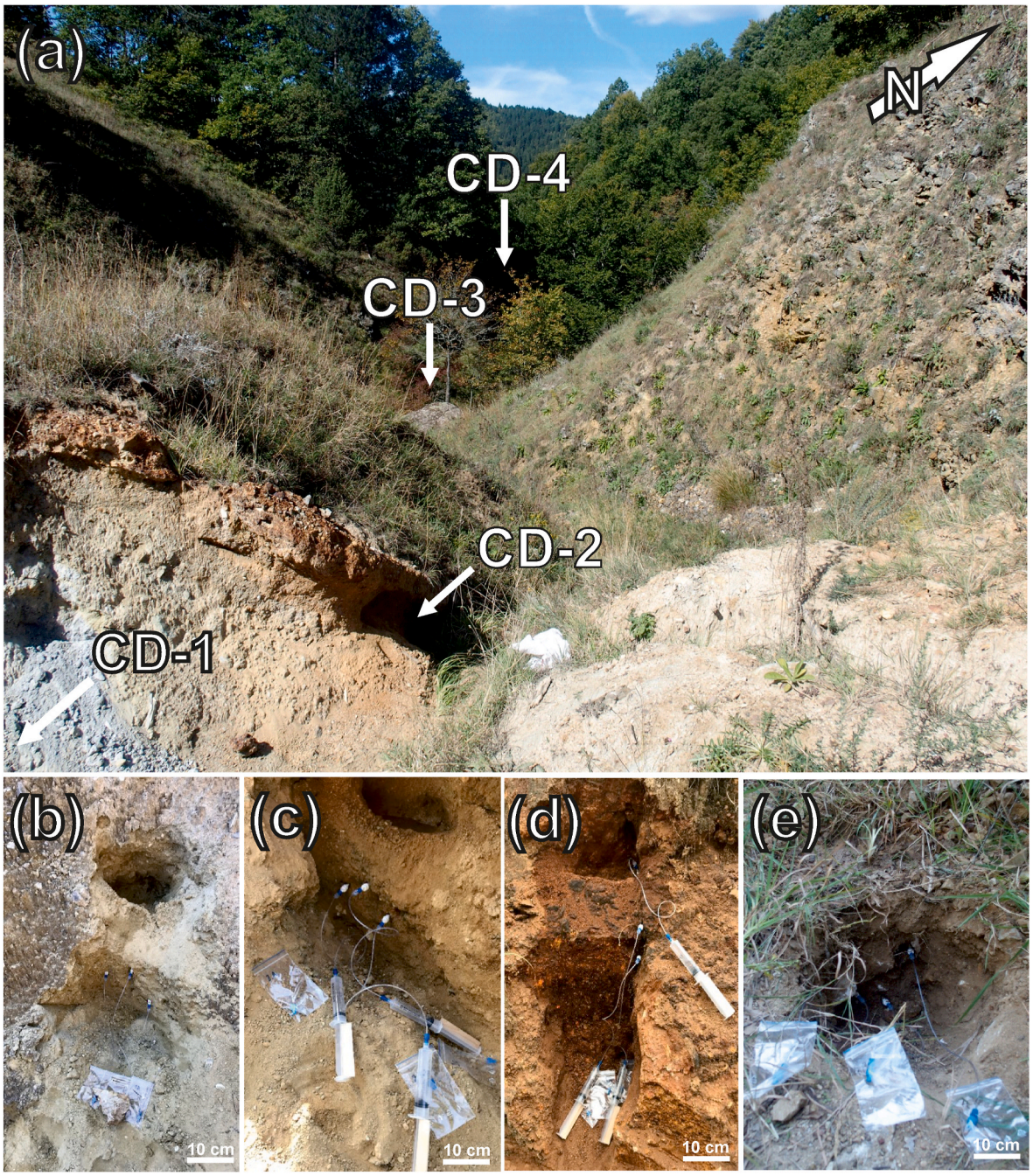

Fig. 2. (a) Overview of the sampling points, (b) sample CD-1, (c) sample CD-2, (d) sample CD-3, and (e) CD-4. View from adit 21 down the small valley, which leads to the Majdanska river.

transported via the Majdanska river to the Crna river, and deposited in its alluvial plain, an area of intensive agriculture activities (Bačeva et al., 2014).

Approximately 25 kg sample was collected in each hole or profile. For the geochemical analyses, around 2 kg of each sample were sealed in plastic bags and transported to the laboratory as such. The rest of the material was sieved using 1 cm-mesh stainless-steel sieves, packed in 30 kg bags and carried to the Majdanska river in order to separate the heavy minerals by panning.

In the laboratory, the dry samples were sieved to the ≤2-mm fraction and homogenized. A part of the latter was further sieved to obtain the ≤0.063-mm fraction. The pH was measured in a 1:2.5 (w/v) solid-deionized water suspension after 1 h of agitation, using a combined pH electrode (SenTix 41, WTW, Germany) and WTW multimeter. The heavy fractions of the samples were further concentrated using sodium metatungstate monohydrate solution (specific gravity 2.80 g/cm^{-3}). Both heavy-grain concentrates and the ≤2-mm fraction were prepared as standard polished sections for subsequent scanning electron microscopy (SEM) with energy-dispersive X-ray spectroscopy (EDX), electron microprobe analysis (EMPA), and Raman spectroscopy.

Mining waste pore solutions (n = 10) were sampled with Macro-Rhizon suction cups (90 mm long and 4.5 mm thick membrane; mean pore size 0.15 μm) that were installed in the mining waste excavations previously used for collection of the solid samples. A total of 10–15 l of distilled water was poured into each of the excavations of the waste/soil profiles (Fig. 2 b-e). The water was absorbed by waste/soil material and after more than 24 h, the water samples were repeatedly collected (over several days) from the outcrops/profiles (usually 20–30 cm below the

surface) from ca. 0.2 m^3 of mining wastes using the Rhizon samplers. Completely wet mining waste materials in the outcrops usually allowed to collect ca. 30 mL of solution.

The temperature, pH, and Eh (redox potential) were determined immediately in the field on sub-samples of pore solutions using a WTW multimeter and combined pH and ORP electrode (SenTix ORP, WTW, Germany). Samples for major cation and trace element analyses were acidified with trace-metal-grade HNO_3; a sample aliquot for aqueous As speciation analysis was preserved by adding 0.1 M EDTA-Na_2 solution to a concentration of 1 mM (Bednar et al., 2002). Sample aliquots for Hg analysis were acidified with trace-metal-grade HCl and stored in pre-cleaned glass vials with PTFE screw caps (Bravo et al., 2018).

2.3. Chemical analyses and geochemical modelling

Major- and trace-element concentrations in the eight selected solid samples were determined by quadrupole ICP-MS (Agilent 7900) and ICP-OES (PerkinElmer Optima 5300 DV). As described in Đorđević et al. (2019), all samples were milled and homogenized. They were pressure-digested at 225 °C in a mixture of 3 mL of 30% suprapure hydrochloric acid (HCl), 1 mL of 65% suprapure nitric acid (HNO_3), and 1 mL of 40% suprapure hydrofluoric acid (HF) in polytetrafluoroethylene (PTFE) vessels using a PicoTrace DAS acid digestion system, following the protocol by Alexander (2008) and Dulski (2001). After sample decomposition, all acid mixtures were evaporated to incipient dryness and redissolved in 5 mL of 64% suprapure HNO_3. This step was repeated twice before all samples were taken up in a mixture of 2% suprapure HNO_3 and 0.001 M HF.

Concentration of major cations and trace elements in the pore waters were determined using ICP-OES (Agilent 5100, USA) and ICP-MS (Thermo Scientific X_{series}^{II}, UK), respectively. The major anions were determined using high-performance liquid chromatography (HPLC; Dionex ICS-2000, USA). Bicarbonate was calculated from alkalinity, measured by microtitration (Schott Titro-Line Easy automatic titrator, Germany) with 0.05 M HCl. Total Hg was determined by cold-vapor atomic absorption spectroscopy (CV-AAS; LECO AMA 254 Hg analyzer, Altec). Arsenic speciation analyses were performed by anion exchange HPLC-ICP-MS (Agilent 8900x ICP MS spectrometer and Agilent 1200 Series LC pump) under standard analytical conditions (Drahota et al., 2017). The intra-assay coefficient (variance between sample replicates) of variation was better than 5% for all analyzed species (arsenite, arsenate, monomethylarsonic acid, and dimethylarsinic acid).

Saturation indices of selected minerals were calculated with the program PHREEQC (Parkhurst and Appelo, 1999). The LLNL database with its implementation of Tl(I)/Tl(III) equilibria was used and augmented with a few data on Tl-containing solids from Wagman et al. (1982). The redox equilibria were calculated from the oxidation-reduction potential (ORP) measured in the field.

2.4. Mineralogical analyses

All SEM-EDX, EPMA, and Raman studies were performed on the polished sections.

Both sieved and untreated samples selected for powder X-ray diffraction (PXRD) were analyzed with a Bruker D8 Advance diffractometer (Cu-*K*α radiation, Lynxeye detector, 40 kV, 25 mA, step scanning from 5° to 85° 2θ, room temperature, step size 0.01° 2θ, dwell time of 1 s per step). The DIFFRAC.EVA software, version 4.2, and the ICDD powder diffraction file PDF-2 were used for peak and phase identification.

Raman spectra were measured with a Horiba LabRam-HR system equipped with an Olympus BX41 optical microscope in the spectral range between 100 and 4000 cm^{-1} (632.8 nm He–Ne laser; 50 × or 100 × objective; N.A. = 0.90; exposure time between 10 and 60 s).

Chemical composition and micromorphology of mineral phases were studied with a JEOL JSM-6610 LV scanning electron microscope (SEM) with tungsten filament (15 kV), equipped with an energy-dispersive X-ray (EDX) detector (Bruker e-FlashHR+, resolution 127 eV) and Bruker Esprit 2.0 software. Spectra were recorded for 60 s and with dead times <5%.

The quantitative chemical composition of the mineral phases was determined by electron microprobe analyses using a JEOL JXA-8230. The operating conditions were set to an accelerating voltage of 15 kV, a beam current of 5 nA, and a beam diameter between 1 and 5 μm. More details on the EMPA analyses can be found in Supplementary materials.

Further chemical information was obtained by energy-dispersive X-ray spectroscopy (EDX) coupled with transmission electron microscopy (TEM). For this purpose, a FEI TECNAI F20 was used, which is equipped with a GATAN GIF Tridiem energy filter and an EDAX APOLLO XII EDX detector. Quantitative chemical analysis using EDX has 10% relative error due to the spectral noise. Tl was identified via the Tl L series (Tl*L*α, Tl*L*β) and vie the Tl *M*-series (Tl*M*α, Tl*M*β, Tl*M*γ, and Tl*M*z peaks). Both are present in the recorded EDX data. The S*K*α peak does overlap with the Tl*M*α peak but quantification was performed by using the Tl*L*α peak. There is no overlap with any constituents of the respective material, neither for the O*K* peak, nor for the Tl*L*α peak.

Table 1
Representative bulk analyses (ICP-MS) of the waste dump material for selected elements. All data are in mg/kg. The complete data set is given in supplementary Table S1.

Sample	Fraction	Mn	Fe	As	Ba	Tl
CD-1	<2 mm	1430	9504	10 030	32.2	717
	<0.063 mm	1713	6145	6986	11.5	726
CD-2	<2 mm	3079	26 960	14 270	78.6	745
	<0.063 mm	2709	16 550	11 330	19.3	563
CD-3	<2 mm	3137	232 900	142 100	175	14 180
	<0.063 mm	3333	182 200	117 300	43.3	17 580
CD-4	<2 mm	3734	47 080	10 510	3352	1066
	<0.063 mm	2505	34 350	9471	511	902

2.5. Chemical extractions

Each of the <2 mm and <0.063 mm sample fractions was subjected to three single chemical extractions (nitrate, phosphate, and oxalate). Nitrate (1 M NH_4NO_3 for 2 h) extraction was used to quantify mobile As and adsorbed/exchangeable fraction of Tl (Gryschko et al., 2005; Vaněk et al., 2020). Phosphate (0.01 M $NH_4H_2PO_4$ for 16 h) extraction was used to quantify adsorbed/exchangeable fraction of As (Drahota et al., 2014). Acid oxalate extraction (0.2 M NH_4 oxalate/oxalic acid at pH 3) was used to quantify the approximate amount of amorphous and poorly crystalline Fe- and Mn-oxides/arsenates and the associated As and Tl contents (Schwertmann, 1964; Drahota et al., 2014; Vaněk et al., 2020). All extractions were performed in duplicate and with procedural blanks. After the extraction procedures, the solutions were filtered through a 0.2-μm nylon membrane filter, diluted, and analyzed for the elements by ICP-OES and/or ICP-MS.

3. Results

3.1. Chemistry of the bulk samples

The complete dataset of major and trace elements in bulk samples is given in the Supplementary materials (Table S1) and representative chemical-analytical data are given in Table 1. Even the lowest concentration of thallium and arsenic in the studied samples (717 mg/kg and 6986 mg/kg, respectively) are much higher than the values recorded even for heavily contaminated industrial soils (Karbowska, 2016).

The analyzed samples show very high concentrations of Tl and As. In

particular, Tl concentration varies between 0.7 and 17.6 g/kg, while the As concentration ranges between 7 and 142 g/kg. The concentration of Fe is highly variable, displaying relatively low concentration (10–47 g/kg), except in CD-3 (233 g/kg). Distributions of these elements in the <2 mm and <0.063 fractions are quite similar (especially for Tl) or display slight enrichment in the coarser fraction (especially Fe and As). The highest Tl and As concentrations have been measured in the Fe-rich sample (Table S1) CD-3, taken from the realgar-rich and lorándite-bearing dump material. It is noteworthy that in the CD-4 (technosol) sample, the concentrations of Tl, As, and Fe are higher than in the CD-1 and CD-2 samples collected from the mixture of mining waste and soil near the entrance of the adit 21. In the same sample, there is also a slight enrichment in the Ba content (3.4 g/kg). As would be expected, the soil sample CD-4 contains more Si, Al, Fe, K, Na, and Ti than the other three samples (bulk XRF data, Table S7). We remind that the sample CD-4 was taken from a spot where the run-off waters bring the waste material from the localities where the other three samples were taken.

3.2. Chemical extractions

The results of single chemical extractions of As and Tl are given in Fig. 3 (the full set of numerical results is given in Supplementary Table S2). The fractions of exchangeable and oxalate-extractable Tl were quite similar in each sample (especially in CD-2 and CD-3) and varied from one site to another between 8 and 61%. The highest fractions of exchangeable (46% and 53%) and oxalate-extractable Tl (40% and 61%)

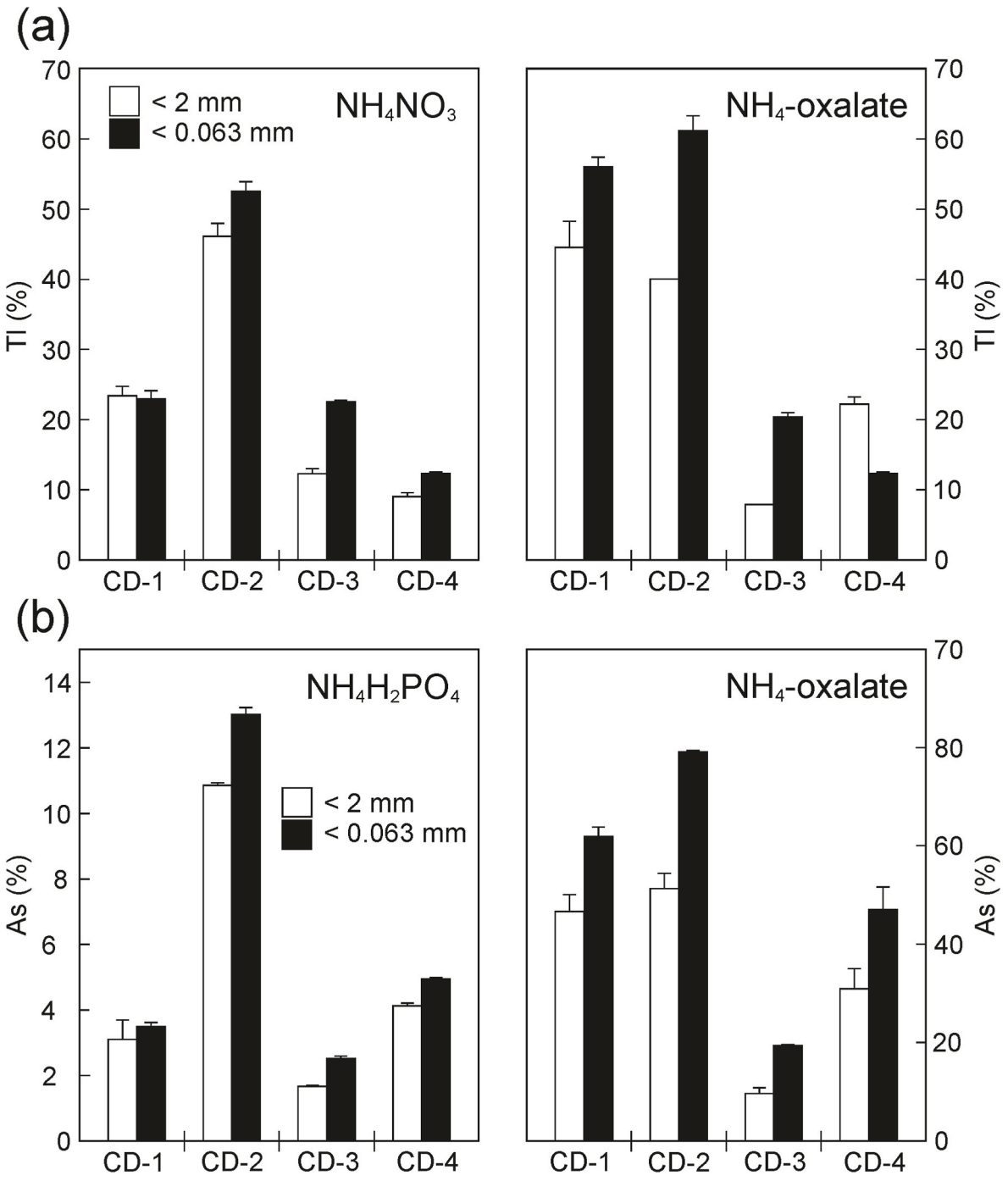

Fig. 3. Thallium and arsenic extraction capacity.

occurred in CD-2 and the lowest exchangeable and oxalate-extractable Tl was documented in CD-4 (9% and 12%) and CD-3 (8% and 20%), respectively. Despite the low fractions of exchangeable and oxalate-extractable Tl in CD-4 and CD-3, the highest extractable concentrations (1130–3960 mg kg^{-1}) were in the CD-3 sample, indicating high mobilization potential of Tl in this sample. The disproportion between low extractability of Tl and high extractable Tl concentrations in CD-3 was due to extremely high Tl concentration in the bulk CD-3 sample compared to the other samples (Table 1). It should be also noted that oxalate-extractable Tl was higher than exchangeable Tl with exception of the CD-3 sample, thus indicating divergent bonding of Tl in this sample compared to the other three samples.

In contrast to Tl, the fractions of exchangeable/adsorbed (phosphate-extractable) and oxalate-extractable As reached different levels. The highest fraction of phosphate-extractable As was in CD-2 (11% in the fraction <2 mm; 13% in the fraction <0.063 mm), while the other samples displayed an exchangeable/adsorbed fraction lower than 5%. The oxalate-extractable As was always higher than 10%, but in most samples (CD-1, CD-2, and CD-4), it was higher than 31%. In combination, CD-3 displays the lowest fraction of mobile (NH_4NO_3-extractable) and exchangeable/adsorbed fraction of As, as well as the As fraction bound to poorly crystalline Fe(III) oxides and arsenates. Nevertheless, the absolute concentrations of exchangeable/adsorbed As and oxalate-extractable As in the CD-3 displayed the highest levels (As_{PO4}: 2360–2950 mg kg^{-1}; As_{OX}: 1.4–2.3 wt%) between the samples due the extremely high total As concentration in the bulk sample (Table 1).

3.3. Chemistry and properties of the pore waters

Concentrations of dissolved Tl and As species and other constituents in pore water are reported in Supplementary Table S3. Pore waters were oxic and their pH was either slightly alkaline (CD-1, CD-2, CD-4: pH 7.4–7.9) or distinctly acidic (CD-3: pH ~3). The dominance of Ca (110–530 mg/L), SO_4 (80–1910 mg/L), and HCO_3 (~170 mg/L in the near-neutral solutions) in the pore water is consistent with the dissolution of dolomite, calcite, and sulfide minerals in the mine waste. High Mg concentration in CD-2 (280–300 mg/L) indicated that dissolution of dolomite probably contributes to the pore-water composition. Slightly alkaline condition of CD-1, CD-2, and CD-4 indicate that the acidity generated by the decomposing sulfides in CD-1, CD-2, and CD-4 has been effectively neutralized by the carbonate gangue minerals, whereas the low pH in CD-3 indicates insufficient neutralization capacity of this sample.

Dissolved Tl and As concentrations are very high in all pore-water samples, ranging from 54 to 660 μg Tl/L and 1–196 mg As/L. Pore-water As occurred almost exclusively as inorganic As(V) (≥99.99 of the total aqueous As) and its concentrations generally correspond to As levels extracted in NH_4NO_3 (Table S2). Very high concentrations of As in the pore-water (9–196 mg L^{-1}) were documented in the slightly alkaline CD-1, CD-2, and CD-4; relatively low dissolved As (<4.8 mg L^{-1}) occurred in the very low-pH CD-3, which was characterized by the highest As concentration in the solid sample (Table 1). It should be noted that aqueous concentrations of Tl were generally similar in all samples indicating lower mobility of Tl in the low-pH and Tl-rich CD-3 compared to other samples.

3.4. Mineralogy of the waste dumps

PXRD studies of the samples used for chemical analyses (Table 2) showed that the dominant minerals in the sample CD-1 (in order of quantity) are calcite, dolomite, quartz, muscovite, orpiment (As_2S_3), pyrite (FeS_2), marcasite (FeS_2), and arseniosiderite ($Ca_2Fe^{3+}_3(AsO_4)_3O_2{\cdot}3H_2O$) (Fig. S1a), in CD-2 these (in order of quantity) are dolomite, gypsum, muscovite, quartz, realgar, marcasite, pyrite, Mn oxides, and orpiment (Fig. S2a), in CD-3 the dominant minerals (in order of quantity) are gypsum, realgar (AsS), muscovite, lorándite ($TlAsS_2$), quartz, dorallcharite ($TlFe^{3+}_3(SO_4)_2(OH)_6$), pararealgar (AsS), and pharmacosiderite ($KFe_4(AsO_4)_3(OH)_4{\cdot}6–7H_2O$) (Fig. S3a). In the soil sample CD-4 the dominant minerals (in order of quantity) are calcite, dolomite, K- and K–Na-feldspars, muscovite, quartz, kaolinite, and orpiment. Since the samples contain on average more than eight phases, especially the PXRD patterns of the heavy fractions (Figs. S1b-4b), PXRD made possible just the identification of the main crystalline phases. For the identification of further, sometimes very widespread minerals, but volumetrically very minor, as well as for the characterization of the amorphous phases, we used a combination of SEM-EDX, EMPA, and Raman spectroscopy on the polished samples (Table 2). In comparison to the most abundant primary minerals, i.e. pyrite/marcasite, orpiment, and realgar, which could be easily distinguished using a binocular microscope, the secondary minerals were not easily recognized during preliminary investigations due to their small to minute size and generally fine-grained nature. In the further text, we focus mostly on the secondary phases. Selected SEM-EDX and EMPA data of the secondary minerals are listed in Supplementary Tables S4 and S5. In the following paragraph, the most important and interesting details of the mineralogical observations of the polished sections are reported.

In the sample CD-3, the main primary source of Tl is lorándite ($TlAsS_2$), which occurs as prismatic crystals and anhedral grains up to 1 mm (also found in the hand specimens) and is frequently intergrown with realgar. It was identified using SEM-EDX, EMPA, and Raman spectroscopy. In the samples CD-1 and CD-4, fangite (Tl_3AsS_4) was identified (SEM-EDX, EMPA) as the dominant primary Tl-source

Table 2
Detailed description of the studied samples and the most abundant minerals according to PXRD, EPMA, SEM-EDX, TEM-EDX, and Raman spectroscopy.

Samples (<2 mm fraction)	Colour: powdered natural samples	Colour: powdered heavy fraction	pH (raw samples)	<63 μm fraction (wt%)	Dominant minerals	Primary ore minerals	Secondary phases
CD-1	pastel yellow-grey	olive-green to grey	8.52	27.9%	calcite, dolomite, quartz, muscovite, kaolinite	pyrite, marcasite, orpiment, fangite	FOHs, arseniosiderite, talmessite, Ca–Mn-arsenate, Mn-oxides, new Tl-arsenates, cinnabar
CD-2	pastel orange-brown	dark-brown-grey	7.34	17.6%	dolomite, gypsum, muscovite, quartz, barite	marcasite, pyrite, orpiment	FOHs, arseniosiderite, Mn-oxides, Ca–Mn-arsenates
CD-3	radiant orange-brown	radiant orange	4.16	7.6%	gypsum, quartz, muscovite	realgar, lorándite, picotpaulite, raguinite	dorallcharite, FOHs, hydroniumjarosite, jarosite, scorodite, Tl-bearing pharmacosiderite, hydroniumpharmacosiderite, natropharmacosiderite
CD-4	light brown-grey	brownish	7.81	3.6%	calcite, dolomite, barite, K-/Na-feldspars, muscovite, "biotite", quartz, kaolinite	marcasite, pyrite, orpiment, fangite	FOHs, arseniosiderite, new Tl-arsenates, Tl_2O, Mn-oxides

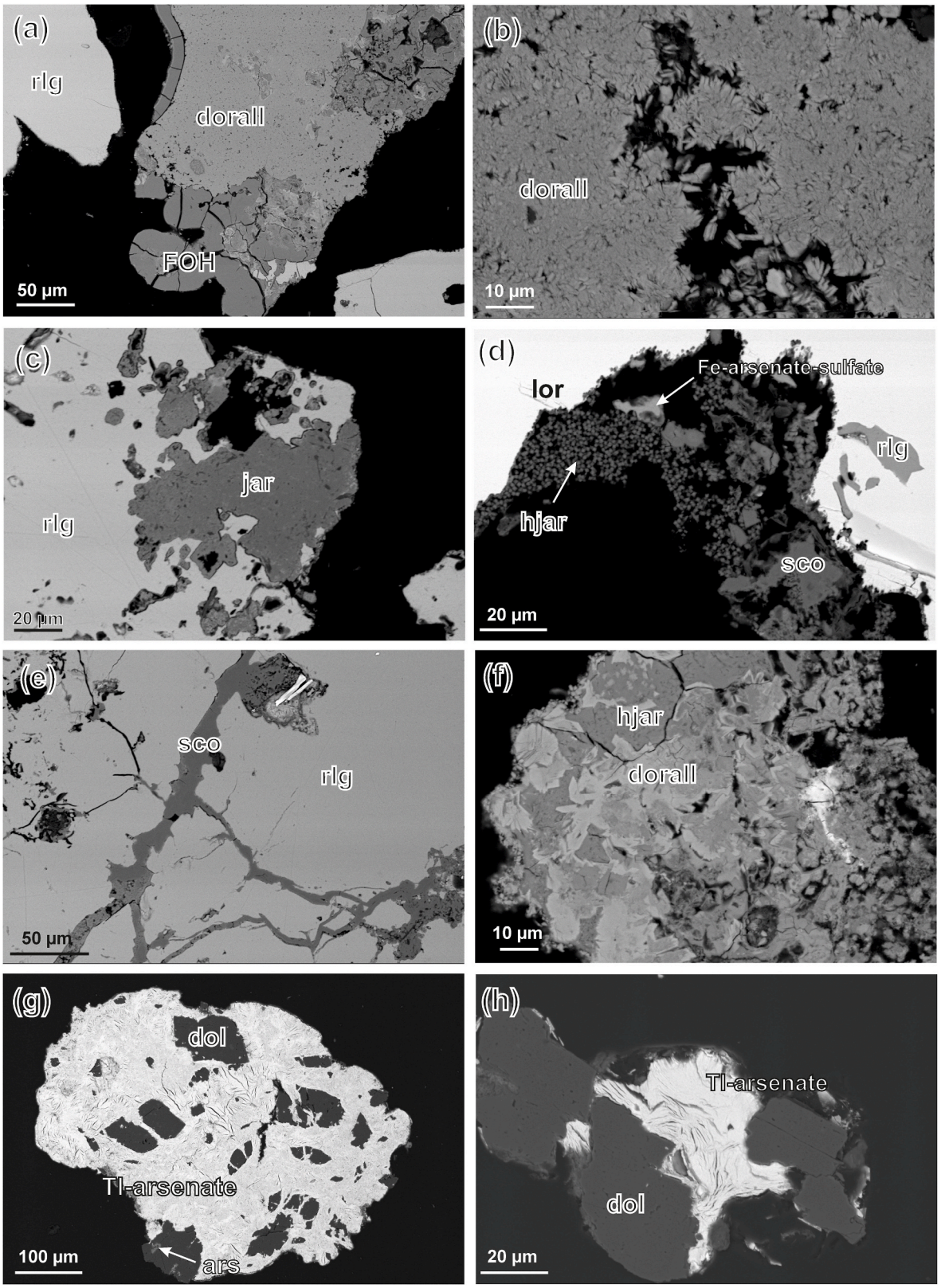

Fig. 4. Back-scattered electron images of polished sections of the mine dump and soil samples. (a) Massive aggregates of dorallcharite (dorall) intergrown with iron oxyhydroxides (FOHs) and realgar in sample CD-3; (b) tiny crystals of dorallcharite (dorall) forming large aggregate, sample CD-3; (c) jarosite (jar) in realgar (rlg); (d) overview of the main primary and secondary minerals in sample CD-3: realgar (rlg), lorándite (lor), hydroniumjarosite (hjar), scorodite (sco), and unindentified Fe-arsenate-sulfate; (e) scorodite filling the cracks of realgar in CD-3; (f) overgrowth of dorallcharite and hydroniumjarosite in CD-3; (g) massive aggregate of two chemically different Tl-arsenates intergrown with dolomite (dol) and arseniosiderite (ars) in CD-4; (h) Tl arsenate intergrown with dolomite in CD-1.

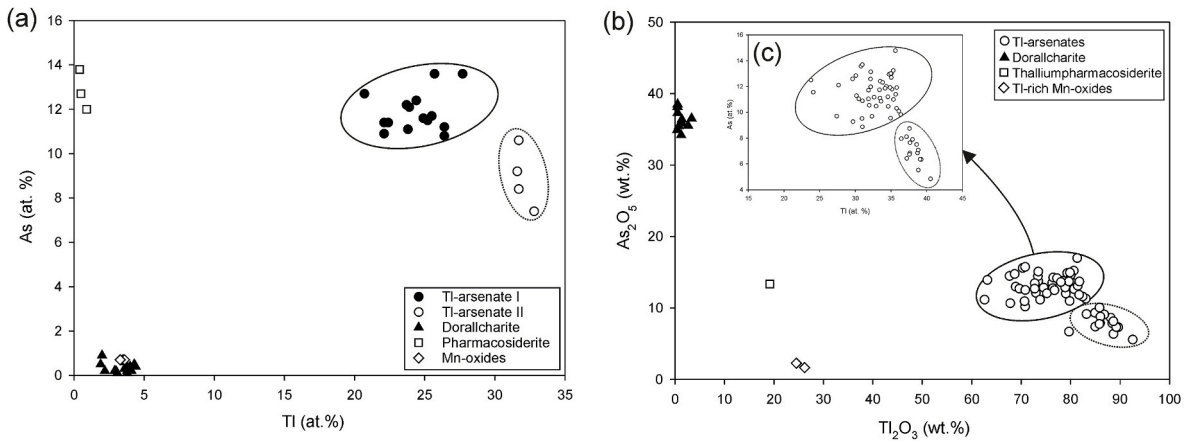

Fig. 5. (a) Variation of Tl as a function of As content in the secondary minerals from Crven Dol (spot data from SEM-EDX analyses); (b) Variation of Tl_2O_3 as a function of As_2O_5 content in the secondary minerals from Crven Dol (data from spot electron-microprobe analyses).

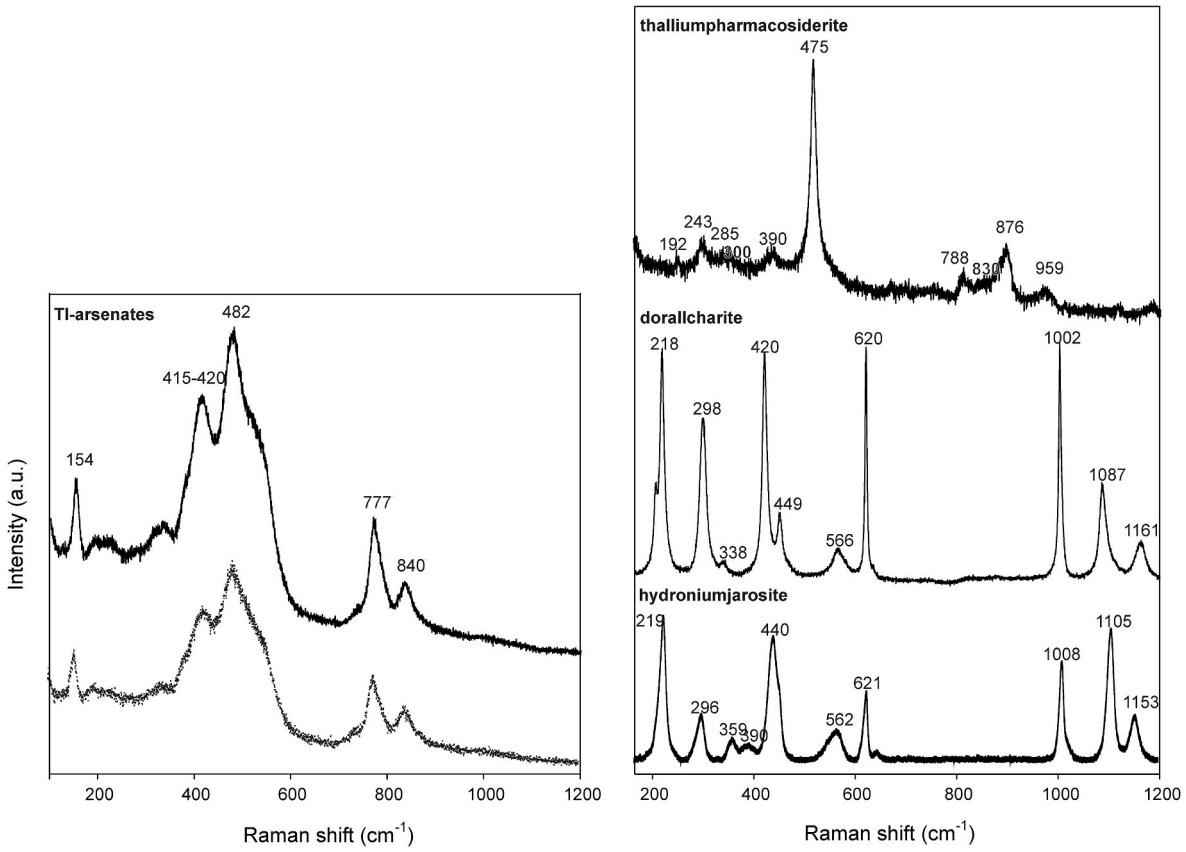

Fig. 6. Raman spectra of secondary thallium minerals from Crven Dol, Allchar deposit.

(Table 2). It crystallizes in narrow cracks and voids of orpiment (Fig. S5a) as subhedral to euhedral grains <20 μm in size. Other Tl sources found only in CD-3, included in either realgar or orpiment, are minor Tl sulfosalts: raguinite ($TlFeS_2$), picotpaulite ($TlFe_2S_3$), and jankovićite [$Tl_5Sb_9(As,Sb)_4S_{22}$] (Fig. S5). They have been identified using both SEM-EDX and EMPA. Besides thallium sulfosalts, the most widespread primary minerals and the main sources of As and Fe are realgar, orpiment, pyrite, and marcasite. They appear either as fresh grains, but are often superficially or strongly altered, showing Fe-oxyhydroxide weathering crusts and crack filling. Very rare and tiny (1–4 μm) cinnabar (HgS) grains (SEM-EDX) are also found (CD-1), as well as rare and small (up to 10 μm), isolated grains of pyrrhotite ($Fe_{1-x}S$) (CD-4) (SEM-EDX).

Using the combination of SEM-EDX and EMPA (in CD-1 and CD-4) we observed that thallium dissolved during weathering is re-precipitated as micaceous subparallel crystals of poorly crystalline thallium arsenates (representing at least one previously unknown mineral species), which form porous aggregates up to 100 μm in interstitial voids, and are often intergrown with dolomite and arseniosiderite (Fig. 4g and h). It appears that two chemically different phases are present. The more common phase shows an atomic Tl:As ratio of ca. 2 and a minor and variable Ca content (2.2–4.1 at%). It was found in both CD-1 and CD-4. In the second, Tl-richer phase, the Tl:As ratio varies from ca. 3.4 to 4.4 and the Ca content is lower, between 0.8 and 1.3 at%

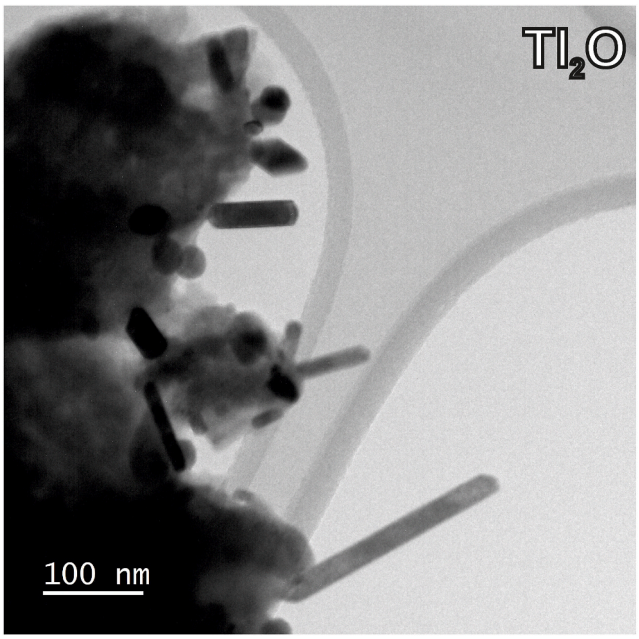

Fig. 7. TEM images of Tl(I) oxide nanocrystals.

(Table S4). These Tl arsenates were further analyzed using Raman spectroscopy. Both SEM-EDX analyses, as well as the EMPA data (Table S4) show two compositional clusters (Fig. 5). Raman spectra of these Tl arsenates (Fig. 6) display broad bands which may be divided in the fingerprint region into two relevant ranges, 350–600 and 700–900 cm^{-1}, both attributed to arsenate tetrahedra showing As–O symmetric bending and stretching modes for the two regions, respectively. No low-wavenumber bands could be unambiguously attributed to modes involving Tl–O vibrations.

The previously unknown Tl arsenates were further investigated using transmission electron microscopy (TEM). Although the analyses were done under cryogenic conditions (−184 °C), the Tl arsenates were found to be extremely sensitive to electron beam irradiation, and diffraction patterns could not be measured due to rapid amorphization. However, intergrown with the Tl arsenates we observed tiny, needle-like crystals up to 25 nm thick and up to 250 nm long (Fig. 7), which we analyzed employing TEM-EDX (Fig. S6). The quantification uses the ZAF approach for thin samples and gives an atomic ratio of Tl:O = 67.8:32.2. Using the theoretical Cliff-Lorimer coefficients of $k_{O/Tl} = 0.0275$ we can conclude that these needles are composed of Tl_2O, thallium(I) oxide. Tl_2O has not been recognized as a natural species yet, although Tl_2O was mentioned, besides unnamed $Tl_2S_2O_3$, unnamed Tl_2SO_4, and avicennite (Tl_2O_3), in Radtke et al. (1985) as one of the alteration products of carlinite (Tl_2S) in a Carlin-type gold deposit in Nevada. During our investigations of the Crven Dol locality, neither carlinite nor avicennite have been found. Nonetheless, very recently we confirmed the presence of avicennite in the waste dumps and oxidation zones of the Sb-rich middle part of the Allchar deposit (Đorđević et al., 2021).

In CD-3, another relatively common Tl-bearing precipitate is dorallcharite (SEM-EDX, EMPA, Raman), crystallizing in the form of tiny, well-formed, tabular crystals that are often grouped into aggregates up to 400 μm in size (Fig. 4a, b,f). Rare and poorly crystallized thallium-pharmacosiderite, $TlFe_4(AsO_4)_3(OH)_4{\cdot}4H_2O$, intergrown with dorallcharite (CD-3), was found and confirmed by EMPA and Raman spectroscopy (Table S5 and Fig. 6). Its Raman spectra (959, 876, 788, 475, 390, 243, and 192 cm^{-1}) compare well with the Raman spectra of pharmacosiderite from the Mokrsko-West gold deposit (Filippi et al., 2007).

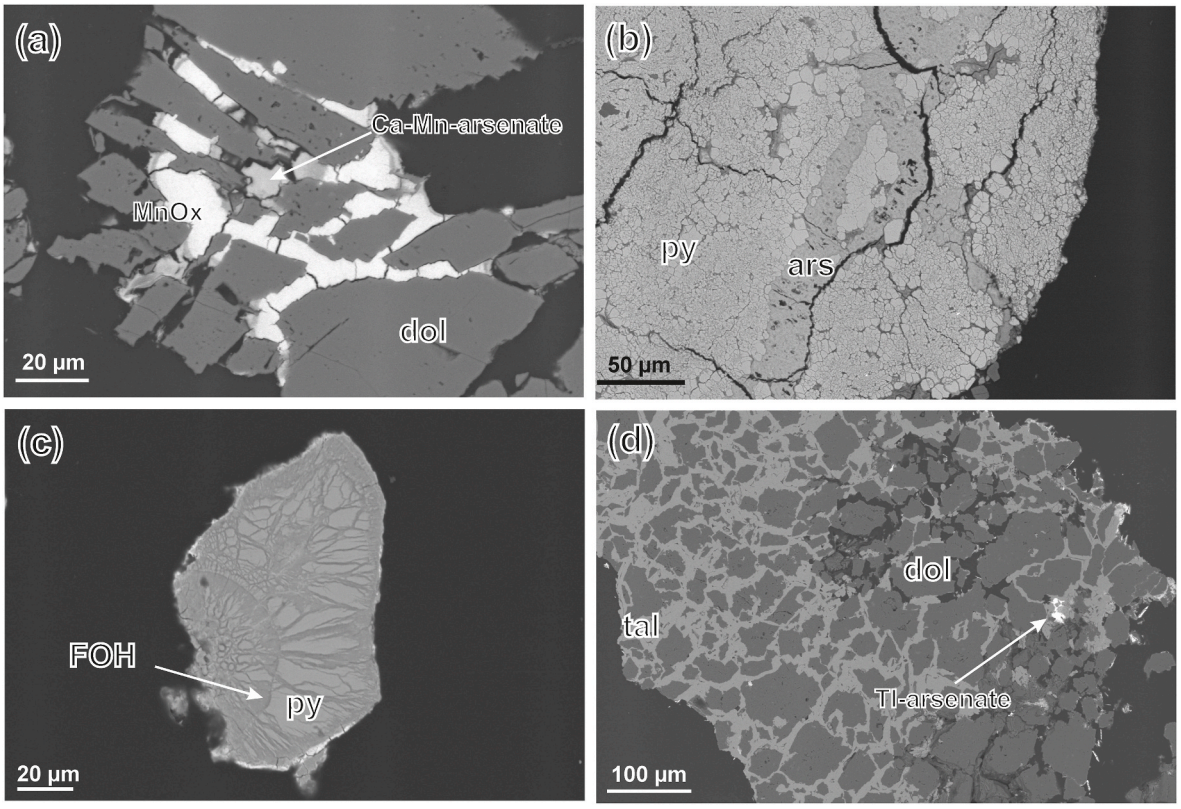

Fig. 8. Back-scattered electron images of polished sections of the mine dump and soil samples. (a) Mn oxide (MnOx) and Ca–Mn-arsenate intergrown with dolomite (dol); (b) arseniosiderite filling the cracks of framboidal pyrite in sample CD-1; (c) pyrite (py) partly altered to Fe-oxyhydroxides (FOHs) in sample CD-1; (d) dolomite (dol) intergrown with talmessite (tal) and with traces of Tl arsenate in sample CD-1.

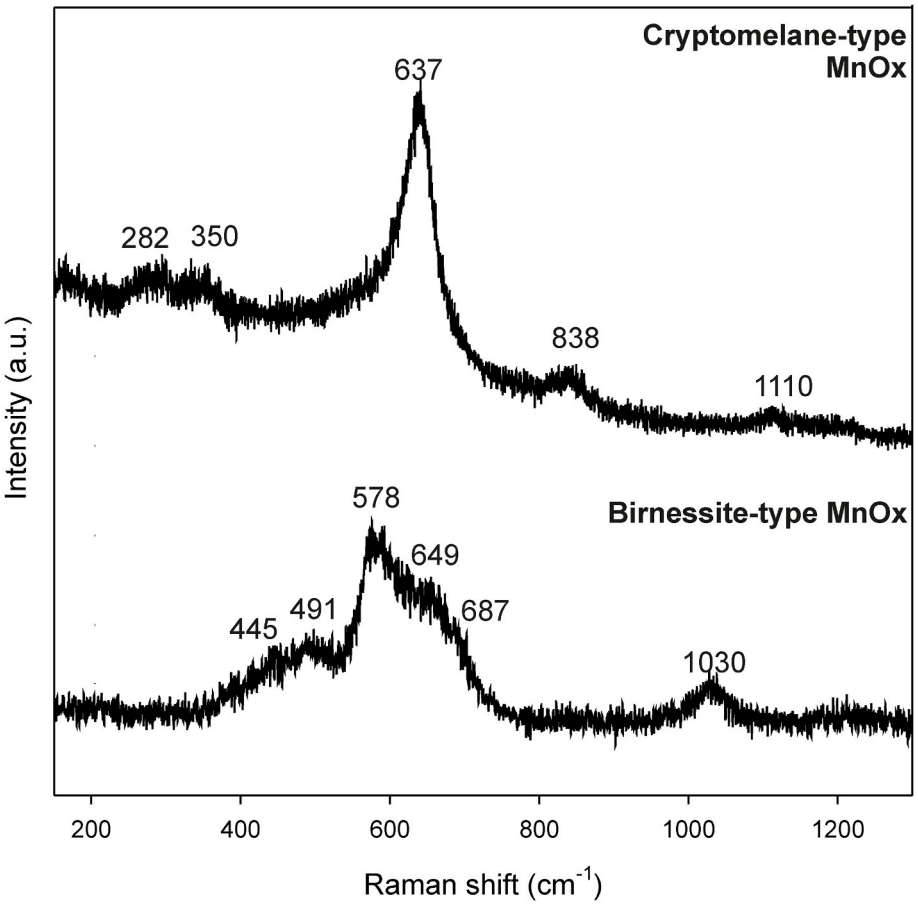

Fig. 9. Raman spectra of Tl-containing fine-grained Mn oxides from Crven Dol, Allchar deposit.

In the CD-2, thallium is also accumulated in cryptomelane [$K(Mn^{4+}_7, Mn^{3+})O_{16}$]-type and birnessite [$(Na,Ca)(Mn^{4+},Mn^{3+})_2O_4 \cdot 1.5H_2O$]-type Mn-oxides (up to 3.6 at% or 26.2 wt%) (SEM-EDX, EMPA). These Mn-oxides fill voids in weathered dolomite grains and appear together with the minor Ca–Mn arsenates (Fig. 8a). In the 550–750 cm^{-1} range (Fig. 9) the Raman spectra show stretching modes of the Mn–O bonds. Previous studies on Mn-oxides (Bernardini et al., 2019; Post et al., 2020, 2021 and references therein) showed that Raman spectroscopy is the only technique that allows an easy discrimination between birnessite- and cryptomelane-type Mn-oxides. It is probable that the Tl-bearing cryptomelane-type Mn-oxides are chemically very similar to the newly described mineral thalliomelane, $Tl(Mn^{4+}_{7.5}Cu^{2+}_{0.5})O_{16}$ (Gołębiowska et al., 2021), but since there are no Raman data available for it yet, it could also be a new Tl-bearing phase.

In CD-3 minor amounts of thallium have also been found by SEM-EDX in pharmacosiderite, $KFe_4(AsO_4)_3(OH)_4 \cdot 6–7H_2O$ (up to 0.9 at%), and jarosite, $KFe^{3+}_3(SO_4)_2(OH)_6$ (up to 0.9 at%) (Table S4). We point out that the whole range of solid-solution compositions was found between jarosite and dorallcharite. Since both pharmacosiderite and thalliumpharmacosiderite were very rare phases, we cannot say with certainty that a complete solid-solution series exists.

Thallium has only very rarely been detectable in dispersed fine-grained secondary Fe-oxyhydroxides (CD-3; EMPA), and only in amounts below 0.1 wt%, close to the detection limit.

In addition to the strong association of As(V) with Fe-oxyhydroxides (FOH) and in the form of the aforementioned new thallium arsenates, As is also stored in a variety of crystalline arsenates. Among these, the dominant phase is arseniosiderite, $Ca_2Fe_3(AsO_4)_3O_2 \cdot 3H_2O$ (SEM-EDX, EMPA). Its fine-grained aggregates are intergrown with strongly weathered Fe-sulfides (Fig. 8b). Apart from CD-3, it frequently occurs in all other samples. Its Raman spectra (388, 858, and 936 cm^{-1}) compare well with the Raman spectra of arseniosiderite from the Smolotely-Lišnice (Drahota et al., 2018), showing Raman bands at 392, 859, and 936 cm^{-1}. Arseniosiderite sometimes contains slightly elevated amounts of Tl_2O_3 (up to 2.4 wt%; Tl assumed to be trivalent and substituting for Fe^{3+}) and Mn (between 1.3 and 2.8 wt% MnO, possibly also as Mn_2O_3), mostly in CD-2 and CD-4 (Table S5).

The second most widespread arsenate is scorodite, $FeAsO_4 \cdot 2H_2O$, found exclusively in sample CD-3 (SEM-EDX, EMPA) as aggregates composed of tiny crystallites. It generally contains very minor amounts of Tl_2O_3 (up to 1.9 wt%; Tl assumed to be trivalent and substituting for Fe^{3+}), P_2O_5 (up to 1.9 wt%), and SO_3 (up to 2.2 wt%).

Another frequently occurring arsenate is talmessite, $Ca_2Mg(AsO_4)_2 \cdot 2H_2O$ (Fig. 8d). It was found in CD-1 and CD-4 (SEM-EDX, EMPA) and is usually intergrown with superficially weathered dolomite, from which it derived its Ca and Mg contents. In the region of the arsenate stretching vibrations (700–900 cm^{-1}), the Raman spectra of talmessite from Crven Dol (Fig. S7) are characterized by four prominent bands at 876, 837, 815, and 785 cm^{-1}. The low-wavenumber region with As–O stretching, bending, and lattice modes is more complex. These spectra compare well with talmessite spectra reported by Frost (2009).

Rare Ca–Mn arsenates were identified tentatively (SEM-EDX, EMPA) as wallkilldellite, $Ca_2Mn^{2+}_3(AsO_4)_2(OH)_4 \cdot 9H_2O$, or manganlotharmeyerite, $Ca(Mn^{3+},Mg)_2(AsO_4)_2(OH,H_2O)_2$. They contain small amounts of Tl_2O_3 (up to 1.8 wt%) and were detected as minor phases in CD-1 and CD-2 (Table S5). They are either intergrown with dolomite and Mn-oxides or they appear as fine-grained alteration rims around altered orpiment, or they fill cracks in orpiment (Fig. 8a). The recording of Raman spectra of these Ca–Mn arsenates using various laser

excitations (473/532/633 nm) failed. This may suggest that these phases are poorly crystalline.

Apart from the widespread dorallcharite, in CD-3 we found (SEM-EDX, EMPA) fine-grained aggregates of hydroniumjarosite, $(H_3O)Fe^{3+}{}_3(SO_4)_2(OH)_6$ (Fig. 4d), and also Tl-bearing (up to 0.9 at%) jarosite, $(K,Tl)Fe^{3+}{}_3(SO_4)_2(OH)_6$ (Fig. 4e).

Iron oxyhydroxides (FOHs) are the predominant secondary phases in CD-3. They represent weathering products of Fe-sulfides and fill cracks and voids of the primary Fe-sulfide grains or appear in the form of massive fine-grained aggregates. Chemically, they are heterogeneous and nearly always contain large amounts of arsenic, with up to 16 wt% As_2O_5 (Table S5). They very rarely contain thallium and if, then mostly less than 0.4 wt% Tl_2O_3. Some of the As-bearing FOHs were identified as goethite by Raman spectroscopy (Fig. S7), but most of them are poorly crystalline and could not be more closely identified. However, the Raman data demonstrated that they contain adsorbed As(V) (Fig. S7). Such an extreme difference in As and Tl concentrations emphasizes the well-known ability of FOHs to adsorb arsenate anions, and indicates that thallium, either as Tl(III) or Tl(I), is hardly incorporated into or adsorbed onto them.

In contrast to FOHs, minor Mn-oxides, which are found in all samples except CD-3, display a strong ability to adsorb or incorporate Tl ions. These Mn-oxides form gel-like crusts and are often intergrown with dolomite and Ca–Mn arsenates (Fig. 8a). They contain up to 3.6 at% of Tl (SEM-EDX).

3.5. Saturation indices of the pore waters

Saturation indices (SI) in pore waters taken at selected localities in Allchar were calculated with the PHREEQC package (Parkhurst and Appelo, 1999). The results are summarized in Table S6.

In these solutions, the concentration of sulfate appears to be controlled by gypsum whose SI are near or slightly below 0. Concentration of arsenic appears to be controlled by FOHs. Saturation indices for scorodite are also near 0 but it is unlikely that the pore waters, most of them near-neutral, would precipitate this mineral, typical for strongly acidic environments. Arseniosiderite is strongly supersaturated (SI 4–5 in most samples) and should therefore precipitate. For Sb, the solutions are strongly supersaturated with respect to tripuhyite (SI $>$ 3) and undersaturated with respect to soluble antimonates, such as brandholzite (SI 6 -12 in most cases). Hence, they should precipitate tripuhyite but the formation of the minerals is known to be kinetically hindered. The severely limited thermodynamic data for Tl phases give no answer as to the source and speciation of this element. The solutions are significantly undersaturated with respect to both Tl_2O and Tl_2O_3 (avicennite) and also with respect to Tl_2SO_4. Much more soluble Tl reservoirs must be responsible for the high observed solubility of this element.

4. Discussion

4.1. Mineralogical evolution and redistribution of elements

The nature of secondary Tl and As species is strongly influenced by the type of primary mineralization and by the presence or absence of pH-buffering carbonate minerals. Secondary minerals result from the weathering of iron, arsenic, antimony, and thallium sulfides and sulfosalts. The chemically simple primary sulfidic mineralization underwent weathering under natural, oxidizing conditions, which led to the redistribution of the major elements Fe, As, Tl, and S. In contrast to the middle part of the Allchar deposit, where we measured Sb concentrations of up to 16 500 mg/kg, in the northern part of the deposit, the maximum measured amount of Sb was 89 mg/kg, and Sb was found only in traces (~0.2 at%) in Mn-oxides. In the carbonate-rich samples Fe mostly enters Ca–Fe arsenates and FOHs. Dissolved arsenic is usually captured in various crystalline arsenates (i.e. arseniosiderite, talmessite). Arseniosiderite is known to dissolve congruently and substantially in oxalate extractions (Drahota et al., 2018). In CD1 and CD2, oxalate extracts contained high concentrations of Ca, Mg, and nearly stoichiometric molar ratio of As and Fe (0.8–1.3). These findings can be ascribed to the dissolution of arseniosiderite and talmessite and suggest that these phases capture roughly 50% of the total As (Table S2). The presence of arseniosiderite in these samples is in good agreement with available thermodynamic and stability data: the mineral readily forms from solutions with highly variable compositions at a wide pH range from slightly acidic to alkaline conditions, but is stable between pH 3.5 and 7.5 and may replace scorodite when pH is increasing and only small amounts of dissolved Ca is available (Paktunc et al., 2015).

The behavior of Tl during weathering is, in part, remarkable. It mostly enters volumetrically not very abundant, but frequently occurring Tl-arsenates previously unknown from natural environments. These arsenates appear poorly crystalline and chemically heterogeneous, with a Tl:As ratio between 2:1 to 4:1. They do not correspond with any of the several known Tl-arsenate compounds (Schroffenegger et al., 2020). We suppose that we are dealing with partly X-ray amorphous weathering products of Tl- and As-rich precursors under circumneutral conditions (pH of the pore water is between 7 and 8). They bear the potential to re-dissolve and re-precipitate as more stable arsenates and/or oxides. Furthermore, Tl was also precipitated as nano-crystalline and very rare Tl_2O, reported in the literature only once as one of the possible natural alteration products of carlinite (Tl_2S) (Radtke et al., 1985).

The preferential incorporation of Tl into secondary Mn-oxides instead of FOH is explained by the easy insertion of Tl cations into the tunnel-like voids in the crystal structures of many major manganese oxide minerals, especially those of the cryptomelane group (Gołębiowska et al., 2016, 2021; Wick et al., 2019; Trueman et al., 2020; Ruiz-Garcia et al., 2021).

Single extraction results show very high proportion of exchangeable Tl (between 9% and 53%, Fig. 3) in comparison to contaminated soils (generally $<$8%) worldwide (Lee et al., 2015; Voegelin et al., 2015; Vaněk et al., 2016, 2020; Wick et al., 2020). Very high exchangeable Tl fractions corroborate the findings that Tl resides not only in manganese oxides. In these extractions, the NH_4^+ cation can force Tl(I) out from accessible structural sites in secondary sulfate and arsenate minerals such as jarosite (Dutrizac, 1997: Dutrizac et al., 2005) and potentially pharmacosiderite and dorallcharite (Majzlan et al., 2019). In contrast, oxalate has been shown as a fairly selective extractant for Tl(III) due to Tl(III) complexation with oxalate (Voegelin et al., 2015). These findings may indicate elevated proportion of Tl(III) in CD-1 and CD-4 (Table S2). It should be noted that 0.2 M NH_4^+ oxalate extraction would also release some fraction of Tl(I) due to cation exchange of Tl(I) and NH_4^+.

CD-3 is rich in gypsum and its dissolvable Fe was mostly incorporated into abundant FOHs, dorallcharite, scorodite, and rare pharmacosiderite-group minerals. Such kind of secondary mineralogy indicates local acidification during weathering, explained by the weathering of abundant Fe-sulfides, realgar, and lorándite, which are all often strongly corroded in the studied samples. The occurrence of dorallcharite documents locally and temporally acidic conditions during weathering, because this mineral forms only under strongly acidic conditions (pH ~1–2; Alpers et al., 1992). The same holds for scorodite (formation pH 0.2–4.5; Fujita et al., 2009, and references therein). As already mentioned, in CD-3 arsenic is captured via adsorption onto FOHs, but is also incorporated into scorodite, pharmacosiderite-group minerals, and possibly also amorphous ferric arsenate. Tl enters mostly dorallcharite and rarely has been found as thalliumpharmacosiderite, Tl-bearing pharmacosiderite, and natropharmacosiderite (up to 0.9 at%). The secondary mineralogy of CD-3 is in good agreement with the low pH of the acid pore-water samples (pH ~3) and the fact that it is the only sample containing major realgar. Oxalate-promoted dissolution in this sample releases As and Fe mostly from poorly-crystalline FOHs, because pharmacosiderite-group minerals and well-crystalline scorodite are almost insoluble in oxalate (Drahota et al., 2014, 2018). These facts are supported by very low Mg and significantly higher Fe/As molar ratio

Table 3
Overview of naturally Tl-polluted sites (major mines, deposits, subeconomic mineralizations).

Locality	Host rocks	max. Tl content in soils (mg/kg)	Primary Tl minerals	Secondary Tl minerals	Reference
As–Tl–Sb–Fe mineralization at **Crven Dol**, Allchar deposit, North Macedonia	Triassic carbonates (dolomite and marble) overlain by a Tertiary volcano-sedimentary sequence of tuffs and dolomites	~20 000	*lorándite*, $TlAsS_2$; *fangite*, Tl_3AsS_4; *raguinite*, $TlFeS_2$; *picotpaulite*, $TlFe_2S_3$; *jankovićite*, $Tl_5Sb_9(As,Sb)_4S_{22}$	*unnamed Tl-arsenates; dorallcharite*, $TlFe^{3+}{}_3(SO_4)_2(OH)_6$; thalliumpharmacosiderite, $TlFe_4(AsO_4)_3(OH)_4{\cdot}4H_2O$; *unnamed* Tl_2O; *unnamed Tl(I)-MnO$_x$*; Tl(I)-bearing *jarosite* (up to 0.9 at%); Tl(I)-bearing *pharmcosiderite* (up to 0.9 at%); Tl(I)-bearing *illite*	Janković (1993), Percival and Radtke (1994), Bačeva et al. (2014), Strmić Palinkaš et al. (2018), this work
Lanmuchang Tl–Hg–As mine, China	Permo-Triassic carbonate rocks and siliciclastic sedimentary rocks overlain by quaternary alluvium	~367	*lorándite*, $TlAsS_2$; *christite*, $TlHgAsS_3$; *imhofite*, $Tl_6CuAs_{16}S_{40}$; *raguinite*, $TlFeS_2$	*lanmuchangite*, $TlAl(SO_4)_2{\cdot}12H_2O$; Tl(I)-bearing *jarosite*, $(K,Tl)Fe^{3+}{}_3(SO_4)_2(OH)_6$); Tl(I)-bearing *hematite*	Dayian et al. (2003), Zhang et al. (2000), Xiao et al. (2003, 2004), Lin et al. (2020)
Nanhua As–Tl deposit, China	Upper Jurassic dolomite, limestone and mudstone	3.6	Tl-bearing *pyrite;* *picotpaulite*, $TlFe_2S_3$; *ellisite,* Tl_3AsS_3; *hutchinsonite*, $TlPbAs_5S_9$	none reported	Zhang et al. (1998, 2007)
Xiangquan Tl deposit, China	Lower Ordovician micritic limestone, marl and mudstone	6.9	Tl-bearing *pyrite; lorándite*, $TlAsS_2$; *hutchinsonite*, $TlPbAs_5S_9$	*lafossaite*, TlCl	Zhou et al. (2005, 2008), Fan et al. (2014)
Tl–As–Fe sulfide mineralization, **Erzmatt**, Switzerland	Triassic dolomite	~10 000	Poorly known due to very advanced weathering Tl-bearing *pyrite;* possibly *carlinite*, Tl_2S	Tl(I)-bearing *jarosite* (up to 10 wt%); *avicennite*, Tl_2O_3; *Tl(I)-bearing illite*	Voegelin et al. (2015), Herrmann et al. (2018)
Pb–Zn–As–Tl–Ba-mineralization, **Lengenbach**, Binn Valley, Switzerland	Triassic metadolomites, metamorphosed under upper-greenschist to lower-amphibolite facies conditions	n.d.	34 Tl sulfosalts (24 type-locality Tl minerals are summarized in Raber and Roth, 2018)	none reported (hardly developed weathering zone)	Hofmann and Knill (1996), Roth et al. (2014), Raber and Roth (2018)
Jas Roux As–Sb–Tl deposit, France	Silicified metamorphosed Triassic sediments (dolomite, limestone)	n.d.	*pierrotite*, $Tl_2(Sb,As)_{10}S_{16}$; *parapierrotite*, $TlSb_5S_8$; *boscardinite*, $TlPb_4(Sb_7As_2)S_{18}$; *chabournéite*, $Tl_4Pb_2(Sb,As)_{20}S_{34}$; *écrinsite*, $AgTl_3Pb_4As_{11}Sb_9S_{36}$; *routhierite*, $Tl(Cu,Ag)(Hg,Zn)_2(As,Sb)_2S_6$	*dorallcharite*, $TlFe^{3+}{}_3(SO_4)_2(OH)_6$ not well studied since locality is in National Park (permit necessary)	Johan and Mantienne (2000), Boulliard et al. (2010), Bourgoin et al. (2011)
Monte Arsiccio Ba–Fe mine, Tuscany, Italy	Hydrothermal baryte-iron oxide-pyrite ore at boundary between Paleozoic phyllites and Triassic metadolostone, metamorphosed under greenschist-facies conditions	n.d.	Tl-bearing *pyrite; arsiccioite,* $AgHg_2Tl(As,Sb)_2S_6$; *boscardinite*, $TlPb_4(Sb_7As_2)S_{18}$; *chabournéite*, $Tl_4Pb_2(Sb,As)_{20}S_{34}$; *parapierrotite*, $TlSb_5S_8$; *protochabournéite*, $Tl_2Pb(Sb,As)_{10}S_{17}$; *routhierite*, $Tl(Cu,Ag)(Hg,Zn)_2(As,Sb)_2S_6$	none reported	George et al. (2018), Biagioni et al. (2020)
Carlin gold mine, Nevada, USA	Thin-bedded, laminated silty dolomite and limestone of Silurian-Devonian Roberts mountain formation	n.d.	*carlinite*, Tl_2S; *christite,* $TlHgAsS_3$; *ellisite,* Tl_3AsS_3; *galkhaite,* $(Cs,Tl)(Hg,Cu,Zn)_6(As,Sb)_4S_{12}$; *lorándite,* $TlAsS_2$; *weissbergite*, $TlSbS_2$	*avicennite*, Tl_2O_3; *unnamed* Tl_2O; *unnamed* Tl_2SO_4; *unnamed* $Tl_2S_2O_3$;	Radtke et al. (1978), Radtke (1985)
Tl mineralization of the **Zarshuran** Carlin-like gold deposit, northwest Iran	Precambrian carbonate and black shale formations intruded by weakly mineralized granitoid	n.d.	*lorándite*, $TlAsS_2$; *christite,* $TlHgAsS_3$; *simonite*, $TlHgAs_3S_6$; *galkhaite*, $(Hg_5Cu)CsAs_4S_{12}$ *hutchinsonite*, $TlPbAs_5S_9$	none reported	Mehrabi et al. (1999), Asadi et al. (2000)
Tl mineralization of the **Vorontsovskoe** Au–Hg–As deposit, Northern Urals, Russia	Exocontact of gabbro-diorite-granodiorite massif intruding volcano-sedimentary rocks	n.d.	22 Tl sulfosalts (including 7 type-locality species)	none reported	Murzin et al. (2017)

(~4) in the CD-3 oxalate extracts compared to other samples. As a result, nearly ~10% and ~20% of total As can be bound to poorly-crystalline FOHs in the <2 mm and <0.063 mm fraction of CD-3, respectively (Fig. 3).

4.2. Weathering behavior of thallium in the Tl-rich sulfide environments

Worldwide, a few natural Tl mineralizations cause or could cause severe environmental Tl pollution. The data on the most important Tl-polluted sites (mines, deposits, subeconomic occurrences) are summarized in Table 3. For nearly all of them, there is a large body of data on the primary mineralogy and for some of them there are also environmental data on soil, surface water, and groundwater. On the other side, the nature of the secondary minerals and the mineral-water interactions of these very specific sites, with the exception of the soils at the locality Erzmatt near the village of Buus in the Swiss Jura Mountains (Voegelin et al., 2015; Hermann et al., 2018), soils of the Langmuchang (LMC) Tl–Hg–As mine in the Guizhou Province, China (Lin et al., 2020), and the present study, were not studied yet. At these localities, Tl mineralization is associated with low-temperature hydrothermal ore bodies and the surrounding soils are severely contaminated with both arsenic and thallium. The soils are characterized mostly by near-neutral pH values, buffered by the carbonate bedrock. In Erzmatt, the concentration of geogenic Tl in the soil profiles increases with depth and reaches a maximum value of ~10 000 mg/kg. At LMC, the total Tl concentration in soils ranges from 68.5 to 367 mg/kg. The extractability of Tl in the presence of 1 M NH_4^+ for the Erzmatt soil (4.9% ± 2.4% of the total Tl) is approximately five times lower compared to the exchangeable fraction (25% ± 15% of the total Tl) in our samples, indicating that Tl possesses high mobility and very high bioavailability in the area of this study. The highest mobile concentration of Tl (1750 mg kg^{-1}) in the study area was found in the sample CD-3, displaying the highest level of mobile Tl worldwide.

Mineralogical analyses of the LMC samples showed that Tl mainly occurred in the fine particles (~1 mm) of jarosite and hematite. In the soils of Erzmatt, Tl occurs as abundant avicennite, with variable As (5–11 wt%) and P (1–3 wt%) content, and as a Tl(I)-bearing jarosite, where the extent of Tl(I)-for-K substitution reaches up to ~10%. A spectroscopic study on the Erzmatt samples (Voegelin et al., 2015) documented that Tl(I) is mainly sorbed to illite and Tl(III) bound to Mn-oxides.

In contrast, the Tl- and As-rich Crven Dol locality of the Allchar deposit seems to have the most prominent and the very well-developed secondary Tl mineralization. Depending on the pH values of the soils or waste dump material, the key Tl minerals are either chemically variable Tl-arsenates (at near-neutral pH values) or dorallcharite (under acidic conditions). Besides these phases, the presence of minor thalliumpharmacosiderite and Tl_2O was also detected. In the samples with near-neutral pH values, noteworthy amounts of thallium (up to 3.6 at%) are associated with cryptomelane- and birnessite-type Mn-oxides. Secondary minerals with exchangeable Tl in their structure are responsible for surprisingly high fractions of readily mobilizable Tl that has not yet been documented in the literature.

It is important to note that in the Allchar area it is very probable that there are other Tl-reservoirs in soils, such as Mn-oxides (birnessite, todorokite, cryptomelane, δ-MnO_2) or Tl-bearing illite, as suggested by several laboratory sorption and spectroscopic studies on these phases (Voegelin et al., 2015; Wick et al., 2018, 2019; Cruz-Hernández et al., 2019), but remote from the primary mineralization. However, the focus of this study is Tl-retention through formation of secondary minerals in an area of the extreme Tl and As concentrations. Because of this distinctiveness and also because necessary thermodynamic data are lacking, we are not discussing the reasons for possible preferential formation of the Tl–As phases, relative to Mn-oxides and Tl-bearing illite. For the discussion of other Tl-reservoirs, an X-ray absorption spectroscopy (μ-XAS) study is planned as an additional paper.

5. Conclusions

In this study we identified As and Tl reservoirs in mine waste and soil samples of an extremely Tl-rich area, the Crven Dol locality. Tl speciation differs from that observed elsewhere, which is confirmed by an extremely well-developed secondary Tl-mineralogy.

Pore waters contain high aqueous concentrations of Tl (up to 660 μg L^{-1}) and As (up to 196 mg L^{-1}). Mild extractions mobilized up to 46% of the total Tl (≤1750 mg kg^{-1}) and 11% of the total As (≤2360 mg kg^{-1}), indicating that a large amount of these toxic elements is bound weakly (sorption) to solids and can potentially be easily mobilized into the pore water and biota.

In soil horizons lacking secondary Tl-bearing minerals, Tl(I) adsorption onto micaceous phyllosilicates (mostly illite), followed by Tl (I) and Tl(III) adsorption onto Mn-oxides has previously been identified as the dominant Tl retention mechanism. However, in Tl-extreme environments, when illite and Mn-oxides are either absent or exhausted, Tl minerals (mainly arsenates and sulfates) form and store Tl.

Although the oxidation zones of the majority of naturally As- and Tl-rich localities represent a great threat to surrounding ecosystems, they have not been investigated so far in much detail. Since the treatment of highly As- and Tl-contaminated soils depends on the character of the As- and Tl-bearing phases, it is necessary to fully characterize As and Tl retention through secondary minerals in these areas, in order to build a sound basis for successful remediation and better environmental management of As- and Tl-contaminated soils.

Declaration of competing interest

The authors declare that they have no known competing financial interests or personal relationships that could have appeared to influence the work reported in this paper.

Acknowledgements

This work was supported by the Austrian Science Fund (FWF): [grant number P 30900-N28]. We thank Goran Batić and Andreas Wagner for preparing the polished sections and Peter Nagl for XRF-analysis of the major elements. Reviews by three anonymous reviewers were helpful in improving the manuscript.

Appendix A. Supplementary data

Supplementary data to this article can be found online at https://doi.org/10.1016/j.apgeochem.2021.105114.

References

Aguilar-Carrillo, J., Herrera, L., Gutiérrez, E.J., Reyes-Domínguez, I.A., 2018. Solid-phase distribution and mobility of thallium in mining metallurgical residues: environmental hazard implications. Environ. Pol. 243, 1833–1845.

Aguilar-Carrillo, J., Herrera-García, L., Reyes-Domínguez, I.A., Gutiérrez, E.J., 2020. Thallium(I) sequestration by jarosite and birnessite: structural incorporation vs surface adsorption. Environ. Pol. 257, 113492–113503.

Alexander, B., 2008. Trace Element Analysis in Geological Material Using Low Resolution Inductively Coupled Plasma Mass Spectrometry (ICPMS). Technical Report 18. Jacobs University Bremen, School of Engineering and Science, Bremen.

Alpers, C.N., Rye, R.O., Nordstrom, D.K., White, L.D., Bi-Shia, K., 1992. Chemical, crystallographic and stable isotope properties of alunite and jarosite from acid-hypersaline Australian lakes. Chem. Geol. 96, 203–226.

Amthauer, G., Pavićević, M.K., Jelenković, R., Goresy, A., Boev, B., Lazić, P., 2012. State of geoscientific research within the lorándite experiment (LOREX). Mineral. Petrol. 105, 157–169.

Asadi, H.H., Voncken, J.H.L., Kühnel, R.A., Hale, M., 2000. Petrography, mineralogy and geochemistry of the Zarshuran Carlin-like gold deposit, northwest Iran. Miner. Deposita 35, 656–671.

Bačeva Andonovska, K., Stafilov, T., Matevski, V., 2018. Accumulation of some toxic elements in relation to their mobility in *Centaurea leucomalla* Bornm. Species from the vicinity of an As–Sb–Tl abandoned mine, Allchar, Kozuf Mountain. J. Environ. Prot. Ecology 19, 609–619.

Bačeva, K., Stafilov, T., Šajn, R., Tănăselia, C., 2013. Air dispersion of heavy metals in the vicinity of the As-Sb-Tl abounded mine and responsiveness of moss as a biomonitoring media in small-scale investigations. Environ. Sci. Pollut. Res. 20, 8763–8779.

Bačeva, K., Stafilov, T., Matevski, V., 2014a. Bioaccumulation of heavy metals by endemic viola species from the soil in the vicinity of the As-Sb-Tl mine "Allchar", Republic of Macedonia. Int. J. Phytoremediation 16, 347–365.

Bačeva, K., Stafilov, T., Šajn, R., Tănăselia, C., Makreski, P., 2014b. Distribution of chemical elements in soils and stream sediments in the area of abandoned Sb-As-Tl Allchar mine, Republic of Macedonia. Environ. Res. 133, 77–89.

Balić-Žunić, T., Stafilov, T., Tibljaš, D., 1993. Distribution of thallium and the ore genesis at the Crven Dol locality in Alšar. Geol. Maced. 7, 45–52.

Balić-Žunić, T.B., Moelo, Y., Lončar, Z., Micheelsen, H., 1994. Dorallcharite, $Tl_{0.8}K_{0.2}Fe_3(SO_4)_2(OH)_6$, a new member of the jarosite-alunite family. Eur. J. Mineral 6, 255–263.

Bednar, A.J., Garbarino, J.R., Ranville, J.F., Wildeman, T.R., 2002. Preserving the distributions of inorganic arsenic species in groundwater and acid mine drainage samples. Environ. Sci. Technol. 36, 2213–2218.

Bermanec, V., Palinkaš, L.A., Fiket, Ž., Hrenović, J., Plenković-Moraj, A., Kniewald, G., Boev, I., Boev, B., 2018. Interaction of acid mine drainage with biota in the Allchar Carlin-type As-Tl- Sb-Au deposit, Macedonia. J. Geochem. Explor. 194, 104–119.

Bermanec, V., Paradžik, T., Kazazić, S.P., Venterc, C., Hrenović, J., Vujaklija, D., Duran, R., Boev, I., Boev, B., 2021. Novel arsenic hyper-resistant bacteria from an extreme environment, Crven Dol mine, Allchar, North Macedonia. J. Hazard Mater. 402, 123437.

Bernardini, S., Bellatreccia, F., Casanova Municchia, A., Della Ventura, G., Sodo, A., 2019. Raman spectra of natural manganese oxides. J. Raman Spectrosc. 50, 873–888.

Biagioni, C., D'Orazio, M., Fulignati, P., George, L.L., Mauro, D., Zaccarini, F., 2020. Sulfide melts in ore deposits from low-grade metamorphic settings: insights from fluid and Tl-rich sulfosalt microinclusions from the Monte Arsiccio mine (Apuan Alps, Tuscany, Italy). Ore Geol. Rev. 123, 103589.

Boev, B., Jovanovski, G., Makreski, P., 2012. Geology and mineralogy of Allchar Sb-As-Tl-Au deposit. II. Congress of Geologists of republic of Macedonia. Geol. Maced. 3, 215–232.

Boulliard, J.C., Morin, G., Bourgoin, V., Favreau, G., 2010. Minerals of jas-roux (France): an update. In: 20th General Meeting of the IMA (IMA2010). CD of Abstracts, Budapest, Hungary, p. 422. August 21-27.

Bourgoin, V., Favreau, G., Boulliard, J.-C., 2011. Jas Roux (Hautes-Alpes): un gisement exceptionnel à minéraux de thallium. Le Cahier des Micromonteurs 113, 2–92.

Bravo, A.G., Kothawala, D.N., Attermeyer, K., Tessier, E., Bodmer, P., Amouroux, D., 2018. Cleaning and sampling protocol for analysis of mercury and dissolved organic matter in freshwater systems. Methods (Orlando) 5, 1017–1026.

Carbone, C., Dinelli, E., Marescotti, P., Gasparotto, G., Lucchetti, G., 2013. The role of AMD secondary minerals in controlling environmental pollution: indications from bulk leaching tests. J. Geochem. Explor. 132, 188–200.

Craw, D., Bowell, R.J., 2014. The characterization of arsenic in mine wastes. Rev. Mineral. Geochem. 79, 473–505.

Cruz-Hernández, Y., Villalobos, M., Marcus, M.A., Pi-Puig, T., Zanella, R., Martínez-Villegas, N., 2019. Tl(I) sorption behavior on birnessite and its implications for mineral structural changes. Geochim. Cosmochim. Acta 248, 356–369.

Daiyan, C., Guanxin, W., Zhenxi, Z., Chen, Y., 2003. Lanmuchangite, a new thallium (hydrous) sulphate from Lanmuchang, Guizhou Province, China. Chin. J. Geochem. 22, 185–192.

Đorđević, T., Kolitsch, U., Serafimovski, T., Tasev, G., Tepe, N., Stöger-Pollach, Hofmann, T., Boev, B., 2019. Mineralogy and weathering of realgar-rich tailings at a former As-Sb-Cr mine at Lojane, North Macedonia. Can. Mineral. 57, 10–21.

Đorđević, T., Kolitsch, U., Drahota, P., Majzlan, J., Peřestá, M., Tasev, G., Serafimovski, T., Boev, I., Boev, B., 2021. Tl sequestration in the middle part of the Allchar Sb–As–Tl–Au deposit, North Macedonia. Goldschmidt Abstracts 2021. https://doi.org/10.46427/gold2020.606.

Drahota, P., Grösslová, Z., Kindlová, H., 2014. Selectivity assessment of an arsenic sequential extraction procedure for evaluating mobility in mine waste. Anal. Chim. Acta 839, 34–43.

Drahota, P., Mikutta, C., Falteisek, L., Duchoslav, V., Klementová, M., 2017. Biologically induced formation of realgar deposits in soil. Geochim. Cosmochim. Acta 218, 237–256.

Drahota, P., Kulakowski, O., Culka, A., Knappová, M., Rohovec, J., Veselovský, F., Racek, M., 2018. Arsenic mineralogy of near-neutral soils and mining waste at the Smolotely-Líšnice historical gold district, Czech Republic. Appl. Geochem. 89, 243–254.

DulskiI, P., 2001. Reference materials for geochemical studies: new analytical data by ICP-MS and critical discussion of reference values. Geostand. Newsl. 25, 87–125.

Dutrizac, J.E., 1997. The behavior of thallium during jarosite precipitation. Metall. Mater. Trans. B Process Metall. Mater. Process. Sci. 28, 765–776.

Dutrizac, J.E., Chen, T.T., Beauchemin, S., 2005. The behaviour of thallium(III) during jarosite precipitation. Hydrometallurgy 79, 138–153.

Fan, Y., Zhou, T., Yuan, F., Wu, M., 2014. Geological and geochemical constraints on the genesis of the Xiangquan Tl-only deposit, eastern China. Ore Geol. Rev. 59, 97–108.

Filippi, M., Doušová, B., Machovič, V., 2007. Mineralogical speciation of arsenic in soils above the Mokrsko-west gold deposit, Czech Republic. Geoderma 139, 154–170.

Frost, R.L., 2009. Raman and infrared spectroscopy of arsenates of the roselite and fairfieldite mineral subgroups. Spectrochim. Acta A71, 1788–1794.

Fujita, T., Taguchi, R., Abumiya, M., Matsumoto, M., Shibata, E., Nakamura, T., 2009. Effect of pH on atmospheric scorodite synthesis by oxidation of ferrous ions: physical properties and stability of scorodite. Hydrometallurgy 96, 189–198.

George, L.L., Biagioni, C., D'Orazio, M., Cook, N.J., 2018. Textural and trace element evolution of pyrite during greenschist facies metamorphic recrystallization in the southern Apuan Alps (Tuscany, Italy): influence on the formation of Tl-rich sulfosalt melt. Ore Geol. Rev. 102, 59–105.

Gołębiowska, B., Rzepa, G., Pieczka, A., 2016. Exceptional Tl-bearing manganese oxides from Zalas, Krakow area, southern Poland. Mineralogia 46, 3–17.

Gołębiowska, B., Pieczka, A., Zubko, M., Voegelin, A., Göttlicher, J., Rzepa, G., 2021. Thalliomelane, $TlMn^{4+}_{7.5}Cu^{2+}_{0.5}O_{16}$, a new member of coronadite group from Zalas, southern Poland. Am. Mineral. https://doi.org/10.2138/am-2021-7577.

Gryschko, R., Kuhnle, R., Terytze, K., Breuer, J., Stahr, K., 2005. Soil extraction of readily soluble heavy metals and as with 1 *M* NH_4NO_3-solution – evaluation of DIN 19730. J. Soils Sediments 5, 101–108.

Hermann, J., Voegelin, A., Palatinus, L., Mangold, S., Majzlan, J., 2018. Secondary Fe-As-Tl mineralization in soils near Buus in the Swiss Jura Mountains. Eur. J. Mineral 30, 887–898.

Hofmann, B.A., Knill, M.D., 1996. Geochemistry and genesis of the Lengenbach Pb-Zn-As-Tl-Ba-mineralisation, Binn Valley, Switzerland. Miner. Deposita 31, 319–339.

Hudson-Edwards, K.A., 2016. Tackling mine wastes. Science 352, 288–290.

Janković, S.R., 1993. Metallogenic features of the Alsar epithermal Sb–As–Tl–Au deposit (the Serbo-Macedonian metallogenic province). N. Jb. Mineral. Abh. 166, 25–41.

Janković, S.R., Jelenković, R., 1994. Thallium mineralization in the Allchar Sb-As-Tl-Au deposit. N. Jb. Mineral. Abh. 167, 283–297.

Johan, Z., Mantienne, J., 2000. Thallium-rich mineralization at Jas Roux, Hautes-Alpes, France: a complex epithermal, sediment-hosted, ore-forming system. J. Geosci. 45, 63–77.

Karbowska, B., 2016. Presence of thallium in the environment: sources of contaminations, distribution and monitoring methods. Environ. Monit. Assess. 188, 640.

Lee, J.-H., Kim, D.-J., Ahn, B.-K., 2015. Distributions and concentrations of thallium in Korean soils determined by single and sequential extraction procedures. Bull. Environ. Contam. Toxicol. 94, 756–763.

Lin, J., Yin, M., Wang, J., Liu, J., Tsang, D.C.W., Wang, Y., Lin, M., Li, H., Zhou, Y., Song, G., Chen, Y., 2020. Geochemical fractionation of thallium in contaminated soils near a large-scale Hg-Tl mineralized area. Chemosphere 239, 124775.

Liu, J., Luo, X., Sun, Y., Tsang, D.C.W., Qiu, J., Zhang, W., Li, N., Yin, M., Wang, J., Lippold, H., Chen, Y., Sheng, G., 2019. Thallium pollution in China and removal technologies for waters: a review. Environ. Int. 126, 771–790.

López-Arce, P., Garrido, F., García-Guinea, J., Voegelin, A., Göttlicher, J., Nieto, J.M., 2019. Historical roasting of thallium- and arsenic-bearing pyrite: current Tl pollution in the Riotinto mine area. Sci. Total Environ. 648, 1263–1274.

Majzlan, J., Haase, P., Plášil, J., Dachs, E., 2019. Synthesis and stability of some members of the pharmacosiderite group, $AFe_4(OH)_4(AsO_4)_3{\cdot}nH_2O$ (A = K, Na, 0.5Ba, 0.5Sr). Can. Mineral. 57, 663–675.

Martin, L.A., Wissocq, A., Benedetti, M.F., Latrille, C., 2018. Thallium (Tl) sorption onto illite and smectite: implications for Tl mobility in the environment. Geochim. Cosmochim. Acta 230, 1–16.

Mehrabi, B., Yardley, B.W.D., Cann, J.R., 1999. Sediment-hosted disseminated gold mineralisation at Zarshuran, NW Iran. Miner. Deposita 34, 673–696.

Murzin, V.V., Naumov, E.A., Azovskova, O.B., Varlamov, D.A., Rovnushkin, M.Y., Pirajno, F., 2017. The Vorontsovskoe Au-Hg-As ore deposit (Northern Urals, Russia): geological setting, ore mineralogy, geochemistry, geochronology and genetic model. Ore Geol. Rev. 85, 271–298.

Paktunc, D., Majzlan, J., Huang, A., Thibault, Y., Johnson, M.B., White, M.A., 2015. Synthesis, characterization, and thermodynamics of arsenates forming in the Ca-Fe (III)-As(V)-NO_3 system: implications for the stability of Ca-Fe arsenates. Am. Mineral. 100, 1803–1820.

Parkhurst, D.L., Appelo, C.A.J., 1999. User's guide to PHREEQC (Version 2): a computer program for speciation, batch-reaction, one-dimensional transport, and inverse geochemical calculations. Water-Res. Inv. Rep. 99, 312.

Pavićević, M.K., Cvetković, V., Amthauer, G., Bieniok, A., Boev, B., Brandstätter, F., Götzinger, M., Jelenković, R., Prelević, D., Prohaska, T., 2006. Quartz from Allchar as monitor for cosmogenic ^{26}Al: geochemical and petrogenetic constraints. Mineral. Petrol. 88, 527–550.

Pavićević, M.K., Bosch, F., Amthauer, G., Aničin, I., Boev, B., Brüchle, W., Djurčić, Z., Faestermann, T., Henning, W.F., Jelenković, R., Pejović, V., 2010. New data for the geochemical determination of the solar pp-neutrino flux by means of lorandite mineral. Nucl. Instrum. Methods A621, 278–285.

Percival, T., Radtke, A.S., 1994. Sedimentary-rock-hosted dissemination gold mineralization in the Alšar district, Macedonia. Can. Mineral. 32, 649–655.

Post, J.E., McKeown, D.A., Heaney, P.J., 2020. Raman spectroscopy study of manganese oxides – tunnel structures. Am. Mineral. 105, 1175–1190.

Post, J.E., McKeown, D.A., Heaney, P.J., 2021. Raman spectroscopy study of manganese oxides – layer structures. Am. Mineral. 106, 351–366.

Raber, T., Roth, P., 2018. The Lengenbach Quarry in Switzerland: classic locality for rare thallium sulfosalts. Minerals 8, 409–426.

Radtke, A.S., 1985. Geology of Carlin gold deposit Nevada. U. S. Geol. Surv. Prof. Pap. 1267, 124.

Radtke, A.S., Dickson, F.W., Slack, J.F., 1978. Occurrence and formation of avicennite, Tl_2O_3, as a secondary mineral at the Carlin gold deposit, Nevada. J. Res. U. S. Geol. Surv. 6, 241–246.

Rieck, B., 1993. Allchar, Macedonia. Mineral. Rec. 24, 437–449.

Roth, P., Raber, T., Drechsler, E., Cannon, R., 2014. The Lengenbach quarry, Binn Valley, Switzerland. Mineral. Rec. 45, 157–196.

Ruiz-Garcia, M., Villalobos, M., Voegelin, A., Pi-Puig, T., Martínez-Villegas, N., Göttlicher, J., 2021. Transformation of hexagonal birnessite upon reaction with

thallium(I): effects of birnessite crystallinity, pH, and thallium concentration. Environ. Sci. Technol. 55, 4862–4870.
Schroffenegger, M., Eder, F., Weil, M., Stöger, B., Schwendtner, K., Kolitsch, U., 2020. News about thallium arsenates(V). J. Alloys Compd. 820, 153369.
Schwertmann, U., 1964. Differenzierung der Eisenoxide des Bodens durch Extraktion mit Ammoniumoxalat-Lösung. Z. Pflanzenernähr. Bodenkd. 105, 194–202.
Strmić Palinkaš, S., Hofstra, A.H., Percival, T.J., Borojević Šuštarić, S., Palinkaš, L., Bermanec, V., Pecskay, Z., 2018. Comparison of the Allchar Au-As-Sb-Tl deposit, Republic of Macedonia, with Carlin-type gold deposits. Rev. Econ. Geol. 20, 335–363.
Trueman, D., Downing, B., Ledoux, T., Richards, T., 2020. The Taron cesium–thallium epithermal geyserite deposit, Salta Province, Argentina. Explore 188, 13–19.
Vaněk, A., Grösslová, Z., Mihaljevič, M., Trubač, J., Ettler, V., Teper, L., Cabala, J., Rohovec, J., Zádorová, T., Penížek, V., Pavlů, L., Holubík, O., Němeček, K., Houška, J., Drábek, O., Ash, C., 2016. Isotopic tracing of thallium contamination in soils affected by emissions from coal-fired power plants. Environ. Sci. Technol. 50, 9864–9871.
Vaněk, A., Voegelin, A., Mihaljevič, M., Ettler, V., Trubač, J., Drahota, P., Vaňková, M., Oborná, V., Vejvodová, K., Penížek, V., Pavlů, L., Drábek, O., Vokurková, P., Zádorová, T., Holubík, O., 2020. Thallium stable isotope ratios in naturally Tl-rich soils. Geoderma 364, 114183.
Voegelin, A., Pfenninger, N., Petrikis, J., Majzlan, J., Plötze, M., Senn, A.-C., Mangold, S., Steininger, R., Göttlicher, J., 2015. Thallium speciation and extractability in a thallium- and arsenic-rich soil developed from mineralized carbonate rock. Environ. Sci. Technol. 49, 5390–5398.
Volkov, A.V., Serafimovski, T., Kochneva, N.T., Tomson, I.N., Tasev, G., 2006. The Alshar epithermal Au-As-Sb-Tl deposit, southern Macedonia. Geol. Ore Deposits 48, 175–192.
Wagman, D.D., Evans, W.H., Parker, V.B., Schumm, R.H., Halow, I., Bailey, S.M., Churney, K.L., Nuttall, R.L., 1982. The NBS tables of chemical thermodynamic properties. Selected values for inorganic and C1 and C2 organic substances in SI units. J. Phys. Chem. Ref. Data 11, 371.
Wick, S., Baeyens, B., Fernandes, M.M., Voegelin, A., 2018. Thallium adsorption onto illite. Environ. Sci. Technol. 52, 571–580.
Wick, S., Peña, J., Voegelin, A., 2019. Thallium sorption onto manganese oxides. Environ. Sci. Technol. 53, 13168–13178.
Wick, S., Baeyens, B., Fernandes, M.M., Göttlicher, J., Fischer, M., Pfenninger, N., Plötze, M., Voegelin, A., 2020. Thallium sorption and speciation in soils: role of micaceous clay minerals and manganese oxides. Geochim. Cosmochim. Acta 288, 83–100.
Xiao, T., Chen, J., Hong, B., Xu, H., Yang, X., 2003. Thallium contamination in soils and its environmental impact. Bull. China Soc. Mineral Petrol. Geochem. 22, 140–143.
Xiao, T., Guha, J., Boyle, D., 2004. High thallium content in rocks associated with Au-As-Hg-Tl and coal mineralization and its adverse environmental potential in SW Guizhou, China. Geochem. Explor. Environ. Anal. 4, 243–252.
Zhang, Z., Zhang, X.M., Zhang, B.G., 1998. Elemental geochemistry and metallogenic model of Nanhua As-Tl deposit in Yunnan Province, China. Diqiu Huaxue 27, 269–275 (in Chinese with English abstract).
Zhang, Z., Chen, G., Zhang, B., Chen, Y., Zhang, X., 2000. The Lanmuchang Tl deposit and its environmental geochemistry. Sci. China, Ser. A D 43, 50–62.
Zhang, Z., Zhang, B., Hu, J., Yao, L., Tian, Y., 2007. A preliminary discussion on the bio-metallogenesis of Tl deposits in the low-temperature minerogenetic province of southwestern China. Sci. China E D 50, 359–370.
Zhou, T., Fan, Y., Yuan, F., Wu, M.A., Hou, M.J., Voicu, G., Hu, Q.H., Zhang, Q.M., Yue, S.C., 2005. A preliminary geological and geochemical study of the Xiangquan thallium deposit, eastern China: the world's first thallium-only mine. Mineral. Petrol. 85, 243–251.
Zhou, T., Fan, Y., Yuan, F., Cooke, D., Zhang, X., Li, L., 2008. A preliminary investigation and evaluation of the thallium environmental impacts of the unmined Xiangquan thallium-only deposit in Hexian, China. Environ. Geol. 54, 131–145.